VECC/EQG/99-04
Feb. 1999

A Preshower Photon Multiplicity Detector for the ALICE Experiment

A Technical Document

Institute of Physics, Bhubaneswar

A.K. Dubey, D.P. Mahapatra, B. Mohanty, S.C. Phatak

Variable Energy Cyclotron Centre, Calcutta

Z. Ahammed, Subhasis Chattopadhyay, M.R. Dutta Mazumdar, Murthy S. Ganti, P. Ghosh*, T.K. Nayak, S. Pal, R.N. Singaraju, Bikash Sinha, M.D. Trivedi, Y.P. Viyogi[1]

Panjab University, Chandigarh

M.M. Aggarwal, A. K. Bhati, V.S. Bhatia

University of Rajasthan, Jaipur

A. Bharti, S.K. Gupta, R. Raniwala, S. Raniwala

University of Jammu, Jammu

P.V.K.S. Baba, S.K. Badyal, A. Bhasin, A. Gupta, V.K. Gupta, S. Mahajan, L.K. Mangotra, N.K. Rao, S.S. Sambyal

and the ALICE Collaboration

[1]Contact-person : Address for correspondence :
Variable Energy Cyclotron Centre
1/AF, Bidhan Nagar, Calcutta 700064 (INDIA)
(tel: +91 33 3371230, fax : +91 33 3346871)
e-mail : viyogi@vecdec.veccal.ernet.in

* Financially supported by CSIR, New Delhi.

Abstract

A preshower Photon Multiplicity Detector (PMD) is proposed to be implemented in the ALICE experiment to study event shapes and isospin fluctuations and to measure the electromagnetic transverse energy. The PMD, to be mounted on the magnet door at $\sim$ 6 m from the vertex on the opposite side of the dimuon spectrometer, has fine granularity and full azimuthal coverage in the pseudo-rapidity region $1.8 \leq \eta \leq 2.8$. Charged particles are rejected using a charged particle veto (CPV) in front of the converter. The detector is based on a cellular honeycomb proportional chamber design for both the PMD and the CPV, and has a total of $\sim 2\times10^5$ cells, each cell having 1 sq.cm. area. The honeycomb wall forms a common cathode, operated at a high negative voltage. The signal is read out from the anode wires at ground potential using gassiplex electronics. The PMD will be able to take data in conjunction with the dimuon spectrometer and other high rate detectors. Beam test results for a small prototype using Ar(70%) + CO_2(30%) gas mixture indicate that about 80% of the central volume of the detector cell has uniform efficiency ($\sim$ 95%) for MIP detection. The average number of cells fired by a MIP is close to unity.

Using VENUS events and GEANT simulation along with a neural network algorithm for photon-hadron discrimination, it is found that the event-to-event fluctuation of the measured N_γ/N_{ch} ratio is quite small ($< 3\%$). In the case of the PMD alone in ALICE, one can achieve photon counting efficiency of better than 70% and the resulting photon sample has <20% contamination. By combining the PMD with the FMD, which measures the multiplicity of charged particles, one can study DCC and other effects leading to event-by-event fluctuation in charge-to-neutral ratio. The PMD can also study azimuthal anisotropy and flow, down to very low anisotropy values. It can provide reasonable estimates of global transverse electromagnetic energy. The event-to-event fluctuation of the total E_T^{em} estimated using the PMD is small, with a σ of $\sim$ 7%.

Contents

1 Introduction

Motivation for incorporating a preshower photon multiplicity detector (PMD) in the ALICE setup has been briefly described in the ALICE Technical Proposal [1]. Along with the Forward Multiplicity Detector (FMD) measuring charged particle multiplicity in an overlapping part of the phase space, the PMD will greatly enhance the physics capabilities of the ALICE experiment in the search for disoriented chiral condensates [2]. At the LHC energy large particle multiplicity in an event will bring in a new era of single-event physics. The PMD, with its fine granularity, high efficiency and with full azimuthal coverage extending to one unit of pseudorapidity will be most suited to exploit this useful aspect in the study of event shapes which contain wealth of information on whether the nuclear collision proceeded through the deconfinement transition or not. One can also study azimuthal anisotropy and flow, either by a stand-alone PMD [3] or in conjunction with other detectors. The number of photons falling on the PMD in one unit of pseudorapidity in the forward region will be around 5000, resulting in event-to-event fluctuation of less than 2%. Thus one can study multiplicity and isospin fluctuations [4]. The possibility of obtaining estimates of E_T^{em} should also provide opportunities for the study of collective flow and event-by-event fluctuations in transverse energy.

The preshower PMD has already been employed in the WA93 [5] and WA98 [6] experiments at the CERN SPS and is proposed to be added to the STAR experiment at RHIC [7]. Elliptic flow at the SPS energy has been discovered using the WA93 PMD [3] and large scale fluctuations in N_γ/N_{ch} are being studied in the WA98 experiment.

The PMD in ALICE is proposed to be installed at 5.8 m from the vertex, hanging from the magnet door and covering the region $1.8 \leq \eta \leq 2.8$ on the opposite side of the dimuon spectrometer. This region has been selected to minimize the effect of upstream materials like beam pipe and the ALICE baseline detectors.

Fig. 1 shows the cross-section of the PMD system schematically. This basically consists of a finely segmented plane of sensitive material behind a suitable converter. The converter thickness is selected for maximizing the conversion probability and minimizing the shower overlap as well as hadronic interactions in the converter. Lead converter of 3 X_0 thickness has been found to be an optimum choice. Hadrons are to be discriminated using a charged particle veto (CPV) kept in front of the converter. A second preshower plane behind another 3 X_0 converter will be placed to improve the measurement of E_T^{em} per event using the PMD.

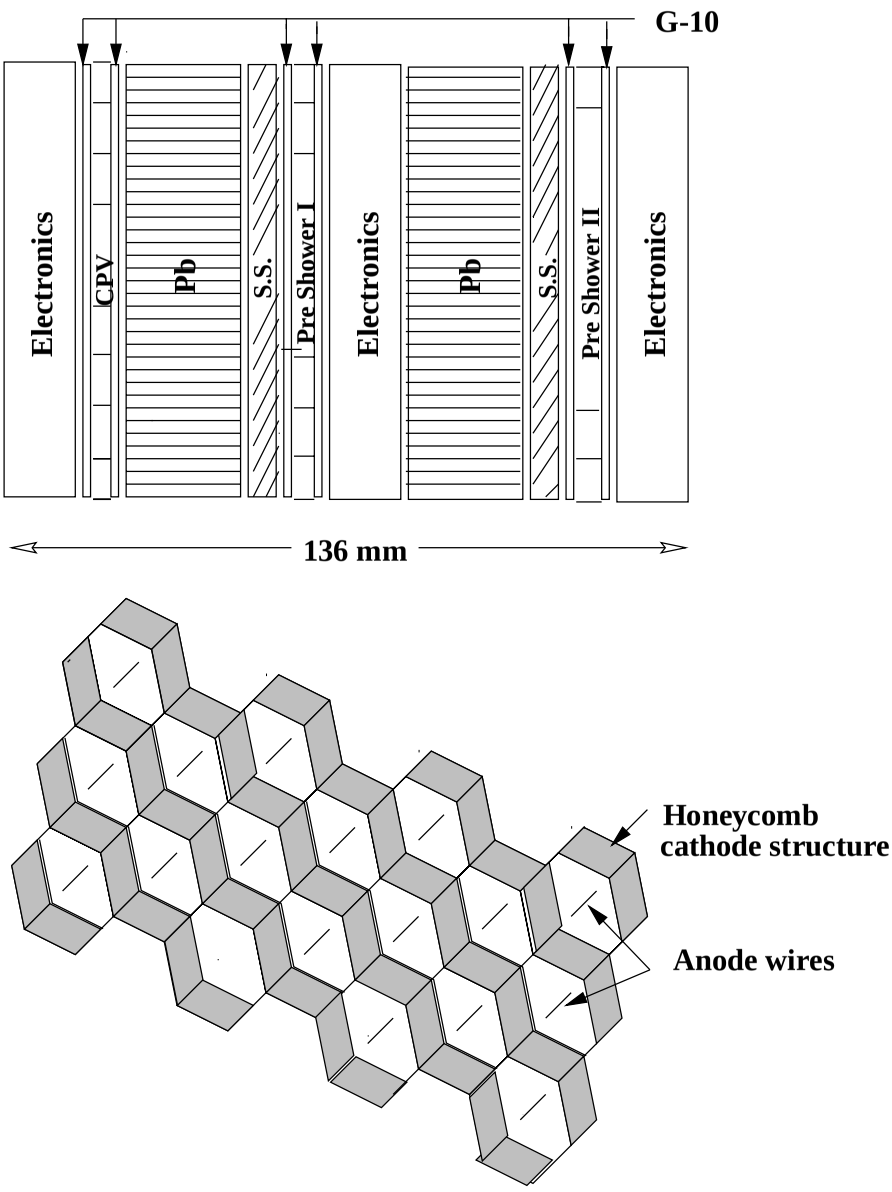

Figure 1: Cross-section of PMD, schematic only, showing the CPV, converter and the two preshower planes. The first preshower plane close to the CPV will have fine granularity for measuring N_γ and the second one further behind another converter will have coarse granularity for estimating E_T^{em}. The bottom part shows the inner detail of the detectors consisting of hexagonal cellular proportional chambers.

The physical parameters of the PMD are summarised in Table I.

TABLE I
Basic Parameters of the ALICE PMD System

Patemeters	value
Distance from vertex	580 cm
η-coverage	1.8–2.8
Active area	10 sq.m.
Inner radius	70 cm.
Outer radius	200 cm.
cell size (area)	1 sq.cm.
Number of channels (PMD + CPV)	200K
$< N_\gamma >$ (VENUS, b $\leq$ 2 fm.)	5100

2 Design and Simulation

2.1 Choice of Detector Hardware

The PMD will use gas as sensitive medium as the other options are either too expensive (e.g., scintillator readout) or not compatible with ALICE baseline detectors (e.g., a silicon option placed close to vertex resulted in increased background into the TPC.) The choice of detector technology for use in a preshower detector has been based on the following considerations :

(a) MIP should be confined preferably to one cell; MIP and photon separation should be good down to lowest possible energy,
(b) total noise level in the detector and readout should be ≤ 0.1 MIP-equivalent,
(c) it should have large dynamic range and possess good linearity to allow estimates of E_T^{em},
(d) it should have stable operation at rates extending upto 10^4 particles/sec/cm^2,
(e) the detector material (gas) should be insensitive to neutrons,
(f) it should be thin so that shower overlap is minimized,
(g) low-energy δ-electrons should be prevented from traveling to cells located farther apart and causing significant cross-talk among adjacent channels. It has been found that in uniform gas volume the preshower extends to a large number of cells [9],
(h) the technology should be amenable to modular design with minimum of dead spaces at the boundaries and should not require staggered layout as it will mean

large volume of air trapped between the detector plane and the converter, resulting in blowing up of showers.

The above considerations rule out the use of conventional gas detector techniques like the cathode pad chambers having large uniform gas volume and pad readout. Apart from cross-talk due to low energy δ-electrons, pad readout tends to broaden the shower due to induced charges at neighbouring pads.

We have therefore selected a design having honeycomb structure and wire readout for the CPV and the PMD as shown in Fig. 1. The basic principle of the detector is similar to that of Ref. [8], but the gas thickness is reduced to our requirements of a preshower detector, and the cells are physically isolated from each other by thin metallic walls to contain δ-rays. The honeycomb geometry is selected because of its closeness to a circular approximation to provide almost circular equipotentials within a cell. This geometry also facilitates close packing of large arrays.

The honeycomb body forms the common cathode and is kept at large negative potential. The individual anode wires in the cells are kept at ground potential and connected to the readout electronics.

2.2 Simulation Results

Details of the simulation scheme and results obtained for deducing the design parameters of the PMD will be presented in a separate document [10]. Here only important results are presented.

2.2.1 Photon counting efficiency and Purity

Counting of photons using a preshower detector is achieved by clustering the hits and applying suitable criteria to reject hadrons. Photons are much more likely to shower in the converter and produce a large signal. Hadrons, on the contrary, produce signal corresponding to a MIP and can be rejected using suitable criteria. The clusters remaining after hadron rejection are mostly from photons and are called γ-like. A fraction of clusters originating from hadrons may escape vetoing and forms part of γ-like clusters. These are termed as contaminants. In addition some photon clusters are also included as contaminants because of the following reasons :

(a) a photon clusters may be split, in that case only one cluster may be assigned to an incident track,

(b) a photon may be deflected by a large angle, its cluster being located at (η, ϕ) value very different from that of the incident track. Such large angle deflections worsen the capability of the PMD for event-by-event physics.

Although the length scales in (η, ϕ) for event-by-event fluctuation studies are not precisely known, very small bins may have problems of too few particles and correspondingly higher statistical fluctuations. The granularity of the FMD, which may be required for the study of isospin fluctuations, is also coarse. Cosmic ray observations by the JACEE collaboration suggest pairing and clustering of tracks at scales $\delta\eta \sim 0.2$ and $\delta\phi \sim 30^o$ [11]. Based on this observation, along with theoretical suggestions [12], we set a lower limit of scale for event-by-event fluctuation studies at $\delta\eta \leq 0.1$ and $\delta\phi \leq 10^o$. Thus all photon clusters having $\delta\eta > 0.1$ or $\delta\phi > 10^o$ are grouped as contaminants.

The photon counting efficiency ϵ_γ and fractional purity of the photon sample f_p are defined by the following relations :

$$\epsilon_\gamma = N_{cls}^{\gamma,th}/N_{inc}^{\gamma} \tag{1}$$

$$f_p = N_{cls}^{\gamma,th}/N_{\gamma-like} \tag{2}$$

where N_{inc}^{γ} is the number of incident photons from the event generator, and $N_{cls}^{\gamma,th}$ is the number of photon clusters above the hadron rejection threshold and satisfying acceptance criteria as discussed above. (1-f_p) is the fractional contamination in the photon sample.

The photon counting efficiency and purity depend on several factors, e.g., the conversion probability, hadron rejection criteria applied, granularity and the track reconstruction efficiency. These also depend on centrality and pseudo-rapidity because of changing particle multiplicity and energy. These are described in the following paragraphs.

2.2.2 Granularity

The granularity of the PMD is determined by the cell size selected for use so that occupancy is within a reasonable limit at the highest particle density expected in ALICE. Very low cell size may lead to artificial splitting of clusters and large cell size may result in high occupancy. To find an optimum cell size, the average

transverse spread of the preshower with 3 X_0 thick lead converter has been estimated for several cell sizes for the case of photons having energy in the range of 1-2 GeV. The average energy of photons given by most event generators in the pseudo-rapidity range under consideration is close to this value. The results are given in Table II. Based on previous simulation results [9], we consider cells of 1 cm^2 area as appropriate choice. For these low energy photons there is no substantial difference in the average number of cells fired if the size is increased from 1 cm to 1.2 cm for square cells.

TABLE II
Average number of cells fired by 1-2 GeV photons after 3 X_0 lead in 8 mm thick Ar + CO_2 gas (assuming square cells).

Cell size (cm)	No. of cells
0.6	5.7
0.8	4.7
1.0	3.7
1.2	3.5
1.5	2.7

2.2.3 PMD in GALICE

The detector configuration implemented in GALICE consists of a set of modules, each having 24 $\times$ 24 cells in a gas volume of 80% Ar and 20% CO_2. Each cell is 1 cm. square with a thin (0.2 mm) metal sheet separating the adjacent cells to minimize cross-talk due to δ-electrons. The square cells have been implemented only for simplicity[2] and for using the clustering software available from WA93/WA98 experiments. The gas volume is bounded on the front and back by 2 mm thick G10 plates. The CPV and the PMD modules are assumed to be identical in granularity. These are placed on opposite sides of the converter consisting of 6 mm thick iron support plate and 15 mm thick lead plate, the two together having a thickness of 3 X_0. The arrangement of modules is shown in Fig. 2 indicating full azimuthal coverage within the specified pseudorapidity region.

[2]The hexagonal cell geometry will soon be implemented in GALICE. The results with such a geometry are expected to be similar to (or slightly better than) the square cells.

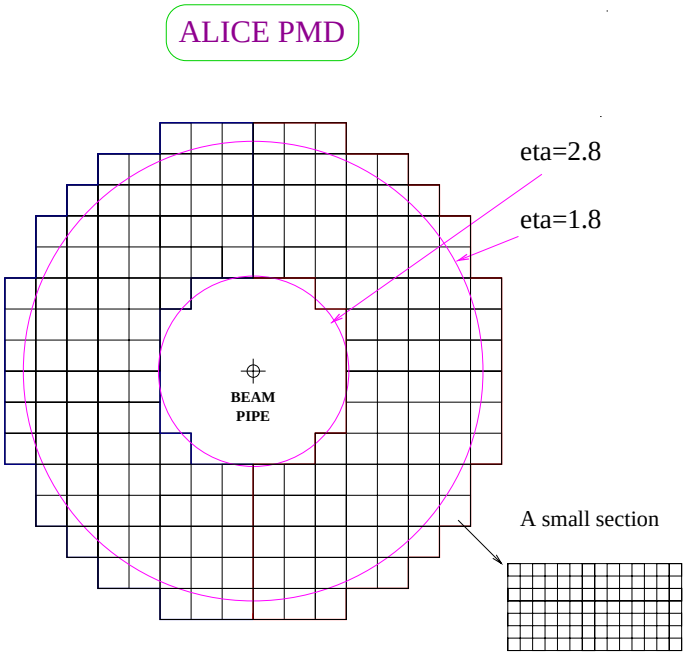

Figure 2: The PMD as implemented presently in GALICE. The inset shows square cells. Each square represents 24 $\times$ 24 cells of 1 cm. square.

2.2.4 Particle density

Simulation has been performed using particles produced in central Pb+Pb collisions (b $<$ 2 fm) given by VENUS event generator and also using parameterized HIJING events for different particle densities. The η-distribution of $\pi^{\pm}$ for VENUS and HIJING are shown in Fig. 3. The $dN/d\eta$ value in HIJING falls off faster than in VENUS and hence HIJING events may give lower occupancy at larger η.

2.2.5 Occupancy

The occupancy depends on the number of cells fired by the incident particle. Fig. 4 shows the number of cells fired by photons and hadrons of different energies. While MIP affects mostly one cell, the number of cells affected by photons varies from 2 to 10, depending on the energy of the incident photon.

The occupancy has been studied for various particle densities. Considering only photons, the occupancy varies from about 3% to 13% over the range studied. This is shown in Fig. 5. Compared to this, the occupancy for central VENUS events is about 16% when all particles are considered.

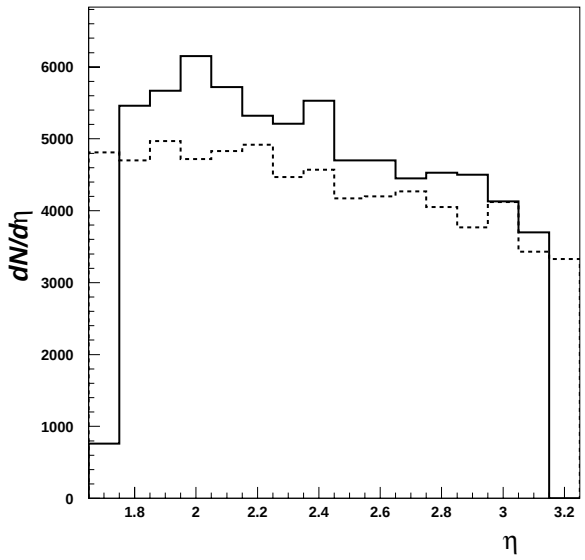

Figure 3: The pseudorapidity distribution of $\pi^{\pm}$ in VENUS (dashed line) and HIJING (continuous line). The $dN_{\pi^{\pm}}/d\eta$ at midrapidity for HIJING and VENUS are 8700 and 7000 respectively.

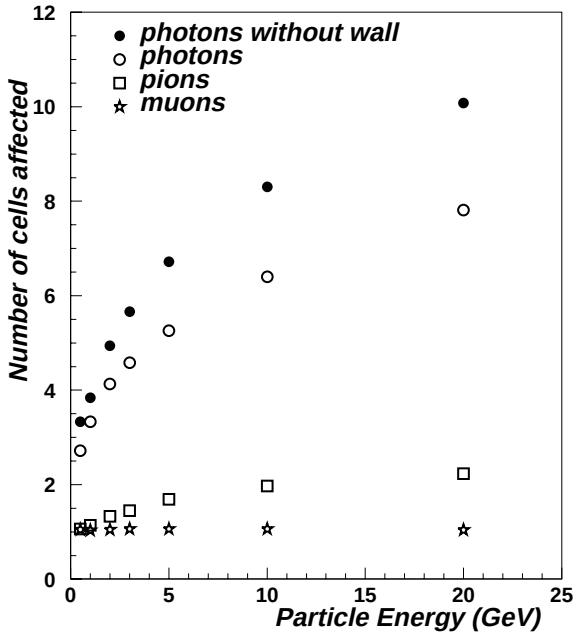

Figure 4: Number of cells affected as a function of particle energy for various cases : asterisks, open squares and open circles respectively denote muons, pions and photons for cells with wall thickness 0.2 mm, filled circles denote photons for cells without wall.

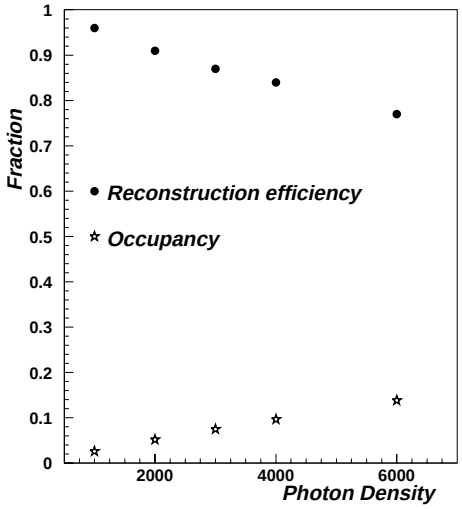

Figure 5: Track reconstruction efficiency and occupancy for various photon densities.

2.2.6 Effect of cell wall

The walls of the honeycomb serve not only to shape the electric field, but also to absorb low energy electrons moving at large angles, which would otherwise fly to neighbouring cells and increase the transverse size of the preshower. Fig. 4 shows the effect of cell wall on the transverse distribution of photon shower. The number of cells affected are reduced by almost 25% by using the cellular configuration with wall of thickness 0.2 mm.

2.2.7 Angular incidence

Using single particle simulation at various incident angles we have estimated the number of cells affected for 2 GeV photons and π^+ over the angular range of the PMD's acceptance. This is shown in Fig. 6. The results indicate that there is no significant dependence within this small angular region. Similar observation has also been made using test data at different angles [14]. This suggests that we can design a detector with flat geometry.

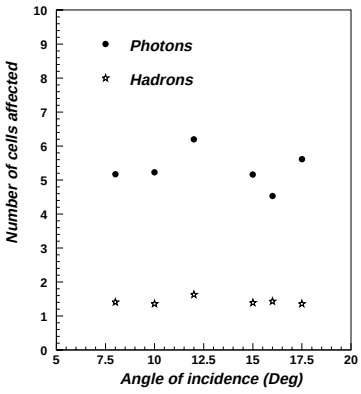

Figure 6: Number of cells affected as a function of incident angle for 2 GeV photons.

2.2.8 Track reconstruction

Track reconstruction efficiency depends on the particle density. This has been studied for various particle densities ranging from 1000 photons to 6000 photons per unit pseudorapidity. For one cm square cells, the reconstruction efficiency varies from 96% at the lowest density to about 80% at the highest density shown in Fig. 5.

The two-track resolution varies from $\delta\eta$=0.01 at the outer edge of the detector to $\delta\eta$=0.03 in the inner regions.

2.2.9 Effect of materials

The effect of upstream materials has been studied in two different ways. In a stand-alone implementation of the PMD geometry, the materials assumed to represent the structural components of the TPC, ITS, FMD and beam pipe are given in Table III. These are described in detail in [10]. In another study, the sub-detectors as implemented in GALICE were switched on one-by-one cumulatively to study their effects.

Effect of materials in stand-alone simulation studies

The selection of a suitable pseudo-rapidity region for the PMD was based on studies using the materials given in Table III and using VENUS event generator. For this study, the PMD was assumed to cover the angular region 6^o–23^o. The

TABLE III
List of materials for stand-alone simulation studies.

Item	description
TPC frame	4 cm thick Al-plate, i.r.=93 cm., o.r.=250cm. at z=250 cm.
	5 cm thick, 5 cm wide Al-rings at 93 cm, 175 cm and 250 cm
	axial and radial honeycomb spokes
ITS frame	6 cm thick 5 cm long Al-tube at z=60 cm.
ITS support	4 cm. thick Al-cone from z=60cm to z=250 cm
FMD	s.s. plates 2 mm thick at given z's.
Structural material	hollow Al-ladders (0.5 cm thick wall, 6 cm square x-section)
	550 cm. long, 50 cm wide, with 23 spokes
	placed at z = 300 cm., 400 cm., 500 cm.
Beam pipe	150 cm section of 0.1 mm thick, 6.0 cm dia Be
	and 0.015 cm thick corrugated SS pipe with flanges

contamination arising due to the upstream materials and beam pipe was estimated for various angular regions as shown in Fig. 7. We find that at angles larger than 18^o, the effect of structural materials of ALICE baseline detectors become significant. We have therefore selected the region 6^o to 18^o for placing the PMD.

The effect of magnet door was also studied using the stand-alone configuration by placing a 1 m thick iron wall 30 cm behind the PMD. The effect on photon tracks was found to be negligible.

Effect of materials from GALICE configuration

Starting from PMD in air, with the coverage restricted to 6^o–18^o, we have switched on different ALICE sub-detectors one-by-one and studied the effect on occupancy. Fig. 8 shows the fractional increase of cell multiplicities in different setups as compared to the cell multiplicity in the case of PMD alone in air. The study has been done for HIJING events with $dN_{\pi^\pm}/d\eta$=5000 within the PMD acceptance. The effect can be readily seen in terms of the increase in the number of cells fired with the inclusion of various detectors in the setup. The main difference in the two configurations lie in the specification of beam pipe, the corrugated structure in stand-alone geometry giving better results.

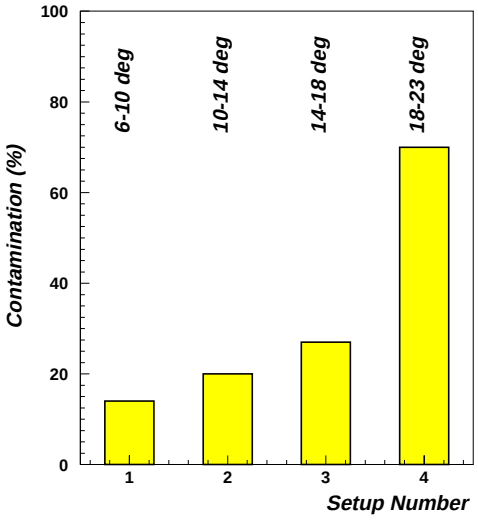

Figure 7: Contamination due to the materials listed in Table III in different angular regions around PMD acceptance.

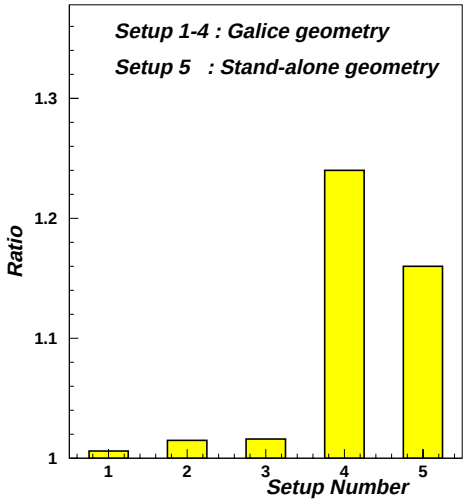

Figure 8: Comparison of the effect of various materials as given in GALICE and also in a stand-alone simulation. The y-axis denotes fractional increase in the number of cells fired as compared to PMD in air. setup 1 : PMD in air + ITS, setup 2 : setup 1 + TPC, setup 3 : setup 2 + FMD, setup 4 : setup 3 + beam pipe. The material is added cumulatively in going from setup 1 to setup 4. Setup 5 shows the result of materials as given in Table III and with VENUS events.

2.3 Photon–Hadron Discrimination

In a preshower detector photons produce large signal after showering but non-showering hadrons produce MIP-like signals. Thus a threshold on the cluster signal should be able to reject most of the charged hadrons. Such a scheme of hadron rejection has been applied in WA93/WA98 PMDs. In this scheme, however, low energy photons also get rejected as their signals fall within the threshold.

In a collider environment photon energies are usually smaller than those in fixed target experiments. Significant number of electrons are also produced in nuclear collisions at the LHC energy. Interesting physics with low p_T particles also makes it necessary to use hadron rejection schemes which are more efficient in retaining low energy photons. We have therefore used a CPV and developed neural network (NN) algorithms for photon-hadron discrimination. The method is described in detail in [13].

The technique consists of standard feed-forward network using the following 21 inputs derived from the preshower and CPV hits of each observed cluster of photons and hadrons :

(i) signal strengths in 9 cells around the cluster maximum of the preshower detector,
(ii) signal strengths in 9 cells in CPV around the cells situated opposite to the cluster maximum mentioned in (i),
(iii) total number of cells affected by the cluster in the preshower part,
(iv) total signal strength of the preshower cluster, and
(v) total signal in 9 CPV cells taken in (ii).

Both hidden layer and functional link approaches of training the network produce similar results.

As the discrimination is to be applied on the observed clusters, after photon conversion and track reconstruction, the results can be better quantified using the variable ϵ_s defined as

$$\epsilon_s = N_{cls}^{\gamma,th}/N_{cls}^{\gamma} \tag{3}$$

where N_{cls}^{γ} is the number of clusters on the preshower plane having photon origin. ϵ_s denotes the fraction of photon clusters which can be filtered after the application of discrimination criteria and is called the photon selection efficiency. The

TABLE IV
Photon selection efficiency, counting efficiency and purity for different configurations of upstream materials.

Material	Evt. Gen.	$< N_\gamma >$	ϵ_s (%)	ϵ_γ (%)	f_p (%)
air only	VENUS	5100	90	70	80
stand-alone	VENUS	5100	82	59	71
GALICE configuration	HIJING	4500	87	58	67

photon counting efficiency ϵ_γ is a convolution of ϵ_s with conversion probability and reconstruction efficiency. The fractional purity f_p of the photon sample is closely connected with ϵ_s, in general ϵ_s drops with increasing f_p.

The results on photon-hadron discrimination are presented in Table IV for three different cases of material specifications. The neural network thresholds have been selected to provide reasonable values of ϵ_s, ϵ_γ and f_p. The use of straight SS section of beam pipe in GALICE worsens the values of ϵ_γ and f_p as compared to stand-alone geometry. The optimum value of the efficiency and purity can be obtained only after all the materials are properly specified and NN threshold adjusted.

3 Prototype Fabrication and Tests

3.1 Prototype Fabrication

A small scale prototype with 96 cells has been fabricated by forming half honeycombs from 0.1 mm thick copper strips and joining the halves to form a row of hex cell structure as shown in Fig. 9. Notches are cut at the corners of each half-cell on both lower and upper edges, as shown in Fig. 9 to facilitate smooth gas flow within all the cells. The honeycomb is then coated with graphite paint to improve the aging properties and suppress after-pulsing. A thin teflon coated wire is soldered at one end of the structure, through which a negative high voltage is applied to the cathode. The layout of the prototype chamber is schematically shown in Fig. 10. A G-10 frame is machined to house the honeycomb, having 0.5 mm more thickness than the honeycomb.

Two printed circuit boards (PCBs) of thickness 1.5 mm each are fabricated having solder islands (1 mm $\times$ 4 mm) at the center of each cell and thin (0.25 mm) tracks leading to 50 pin ERNI edge connectors as shown in Fig. 11. Only

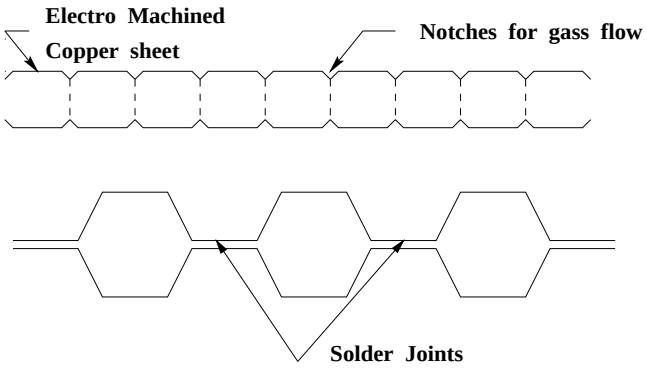

Figure 9: Sketch showing half-row formed from metal pieces

one board has full wiring layout of the tracks, the other having only solder islands to anchor the 20 micron wires. These PCBs have only plain G-10 surface facing the gas side. One PCB is first bonded with epoxy to the G-10 frame. Then the honeycomb is tack-glued to it after checking the alignment. The second PCB is then bonded to the other side of the frame after bringing out the cathode connection.

Gold plated tungsten wires (20 μm dia.) are inserted through the holes of the G10 board using a specially made jig. The jig consists of a small plastic wire spool on an aluminium frame with a hypodermic syringe needle fitted to the frame. The wire is drawn through the capillary of the needle and can be inserted through the PCB holes along with the needle. The needle is withdrawn after tack-soldering the wire onto the rear PCB. The wire can be stretched to a tension of 25-30 gm. using a spring-loaded slider on the spool, before soldering onto the front PCB. The holes are then closed by a high viscosity fast setting (5 min.) epoxy. Two copper clad PCBs are again bonded on the soldered surface of the above mentioned PCBs, with copper on the outer surface to make a proper shielding for the entire readout connections.

Negative high voltage is fed to the honeycomb cathode through a high value (2.2M) non-inductive resistor with a HV decoupling capacitor.

3.2 Test Beam Results

A prototype having 96 cells of area approx. 130 sq.mm. and thickness 12 mm was used for the beam tests in T11 line of the CERN PS. Two sets of microstrip silicon detectors (MSDs) were used for position information on the beam profile.

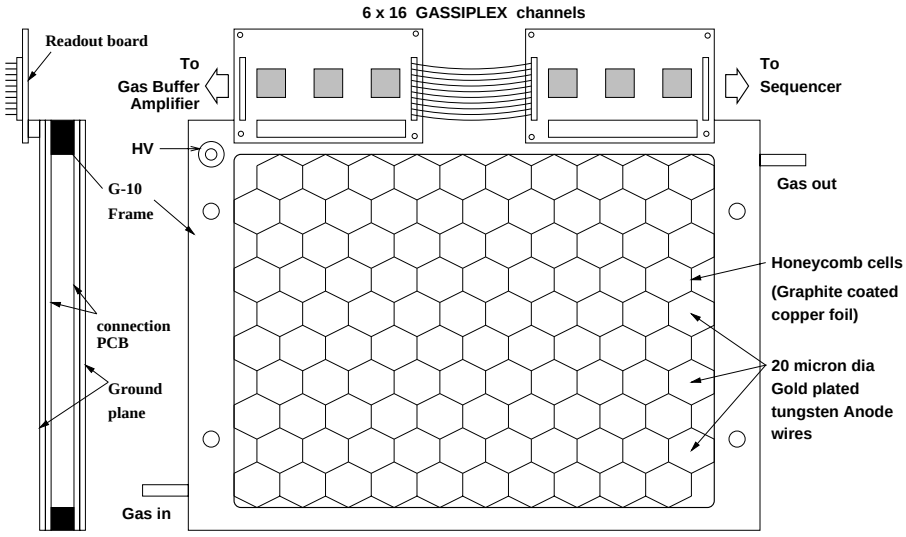

Figure 10: Layout of the hexagonal cells in the prototype chamber. The section at the left shows the G10 frame for the chamber.

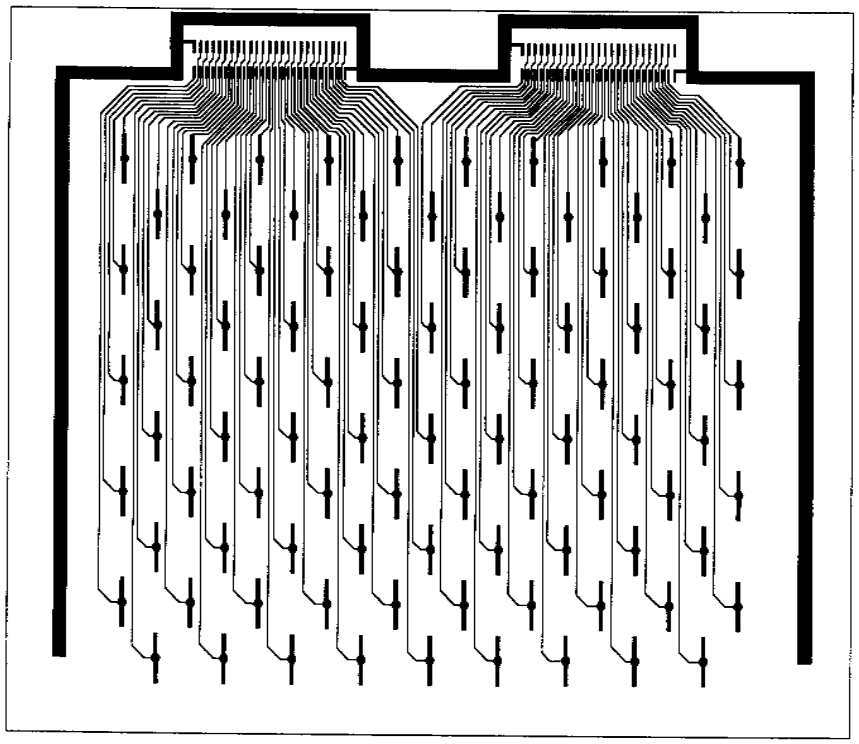

Figure 11: PCB layout for the prototype chamber.

A four-fold coincidence of two pairs of scintillators placed about 1.5 m apart defined the beam trigger. A CO_2 Cerenkov counter was used to obtain electron trigger.

The chamber was tested using 3.5 GeV/c pions to study the response to minimum ionizing particles (MIP) and with 3 GeV/c electrons to study the preshower characteristics. A gas mixture with Ar (70%) and CO_2 (30%) operated at 2450 V was found to give optimum performance. The details can be found in Ref. [14].

3.2.1 Characteristics for MIP detection

Fig. 12 shows a typical MIP spectrum and also the number of cells fired by MIPs. It is seen that MIPs are almost confined to within one cell. This result is very significant, suggesting that the cellular design with wire readout is really able to confine the MIP, and that the cross-talk with neighbouring channels is negligible. Considering the fact that the average number of pads fired in WA98 PMD for the MIP case was 3, the present design represents a marked improvement and should allow us to handle the large multiplicity.

The MIP deposits 3.7 keV energy in 12 mm deep gas medium. Using the central portion of the MIP spectrum we find that the energy resolution of the honeycomb chamber is $\sim$2.2 keV.

By combining the information on beam profile, as registered in the six planes of the MSDs, we have studied the variation of efficiency as a function of position within a cell. It is found that most part of the cell has almost uniform efficiency around 95% and the efficiency at the boundary is somewhat reduced. This can be easily understood from the hexagonal geometry of the cells, where the field configuration at the edges are distorted. Modifications in the design are under investigation.

3.2.2 Preshower characteristics

The preshower ADC spectra, obtained by adding the ADC contents of all the cells in a preshower cluster, are shown in Fig. 13 for the case of 3 GeV/c electrons passing through two different thicknesses of the lead converter as indicated. For this study the gas gain was reduced in order to avoid saturation of the preshower signal in gassiplex. The top part of the figure shows the corresponding MIP spectrum in the central cell where the beam was hitting in the absence of lead converter.

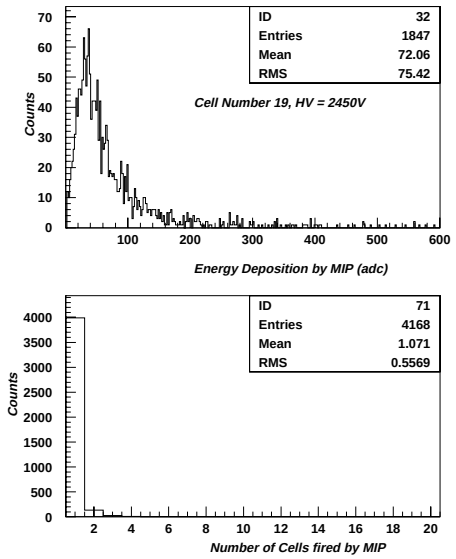

Figure 12: MIP spectrum in a typical cell at 2450 V, and the number of cells fired for MIP

Table V summarizes the results. It is very encouraging to find that the shower spread is confined to fewer number of cells. The somewhat lower value of the average number of cells fired, as compared to that obtained in simulation, is explained by the lower individual cell efficiency. The central cell where the beam hit in the absence of lead converter, had an efficiency of $\sim$ 70%. Combining this value of the average efficiency and the GEANT results we find that the modified simulation result matches the test data. It is therefore expected that the actual occupancy of the detector, after design modification and improvement in efficiency, will be closer to that given by GEANT simulation results. This is a major improvement over the case of WA93/WA98 PMDs [5, 6] where the transverse shower spread in test beam data extended to almost twice the number of pads as given by the simulation, due to the effects of readout electronics.

A comparison of the values of energy deposition in simulation and test beam data for the two cases of converter thickness also indicate that the chamber behaves almost linearly, although more detailed tests are needed to confirm this behaviour.

TABLE V
Preshower Characteristics for 3 GeV/c electrons

item	conv. thick. 2 X_0	conv. thick. 3 X_0
Energy Deposition		
data (ADC)	157	223
simulation (keV)	42.6	66.6
ratio	3.7	3.4
no. of cells fired		
data	2.6	3.1
simulation	3.1	4.2

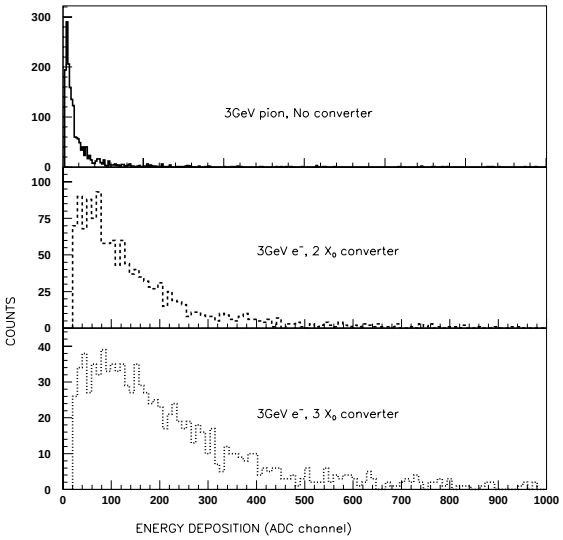

Figure 13: Preshower spectra for 3 GeV/c electrons with two different thicknesses of the converter

4 Engineering Details

4.1 Design Considerations

The PMD, including the CPV, will be designed in the form of a set of supermodules, which will be gas-tight enclosures, containing several unit modules.

4.1.1 Unit module (UM)

The unit module has been designed with following considerations :

(a) ease of mechanical handling, fabrication and assembly,

(b) seamless joining with other modules to form a large uniform array, and

(c) number of channels in multiples of 48 for using multi-chip module (MCM) boards for 3-chip gassiplex readout electronics.

Considering these aspects, a rhombus shaped module having 24 $\times$ 24 cells has been designed (see Fig. 14). This shape has identical boundaries on all four sides and the wall thickness at the boundaries is kept half of that of the inner walls. When such arrays are joined together to form a supermodule, the half-thick boundary walls merge to form a seamless array of hexagonal cells.

4.1.2 Supermodule (SM)

The unit module having 576 cells is a rhombus of side 26 cm. If one uses such modules in large number to cover the entire region of pseudorapidity, the number of cells falling on the borders of the modules will be extremely high. This will cause a large fraction of clusters to split at the boundaries and the efficiency of photon counting will be low. It is, however, not possible to fabricate and assemble a single large unit module because of cost considerations to handle large objects during machining, assembling in clean environments and producing precision moulds of such magnitude. In order to achieve a reasonable compromise between the physical size of a module and the number of cells to minimize the splitting of clusters at the boundaries, we have adopted a scheme of building a supermodule having 3 $\times$ 3 unit modules joined together in a gas-tight enclosure, as shown schematically in Fig. 15.

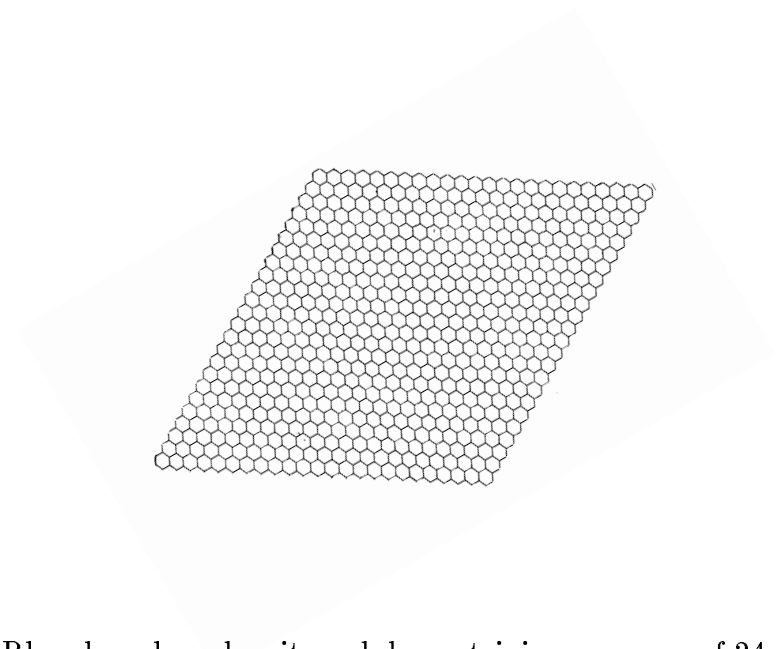

Figure 14: Rhombus shaped unit module containing an array of 24 $\times$ 24 hexagonal cells

4.2 Fabrication of a Unit Module

For the assembly of the unit module, a 576-cell honeycomb cathode structure is first fabricated. Two techniques are under investigation : (a) moulding an engineering plastic into honeycomb and metalizing the surface, and (b) forming metallic honeycombs by a technique similar to that described in the fabrication of the prototype, but using a process which provides mechanical precision and cheap duplication. Final selection of the technique will be done on the basis of time and cost involved and the capability to meet technical specifications.

The honeycomb cathode structure is then dip-coated with high conductivity graphite paint. Two PCB planes are then bounded on either side of the cathode plane. All the anode signal connections are brought out on to the top PCB via high density kapton cables terminating with 50-pin ERNI connectors. Gold plated tungsten anode wires (20 μm dia.) are stretched through the holes on the PCBs, situated at the axial points of the hexagonal cells, using a simple jig with in-built tensioning arrangement. After proper alignment and tensioning, the wires are soldered on the PCBs.

The soldering joints at the ends of the wire are inspected for dry solders using a milli-ohm meter. Defects found at this stage are rectified, wires taken out, fresh one reinserted and soldered.

The unit module will be assembled in class 100 clean environment to pre-

vent dust entering the cells. This is particularly important as, contrary to large area MWPCs and cathode pad chambers, the cell boundaries in the honeycomb chamber design do not allow forced flushing of gases. Thus dust trapped within a cell during assembly may not be easily expelled by the gas flushing operation.

The unit module covered with the PCB planes after assembly will be kept in a sealed cover for transportation and further use during the assembly of the supermodules.

4.3 Assembly of a Supermodule

A supermodule consists of 3 $\times$ 3 array of unit modules housed in a gas-tight enclosure made up of 2 mm thick SS-304 sheets as shown in Fig. 15. The bottom of the enclosure is insulated with thin polyimide film and the top shielding plane has cut-outs for the kapton cables. The kapton ribbon boundaries and the edges of the shielding plane are sealed gas-tight with RTV/epoxy sealant.

Two opposite sides of the SS box module have raised walls to provide anchor points for the HV and gas-feed subassembly boxes. This is schematically shown in Fig. 16. One cell each at the four corners of the supermodule is retained without anode wire so as to allow the bolts to pass through for fixing the SM's onto the support plate.

The following sequence is to be adopted for the assembly of supermodules :

(i) Nine unit modules along with kapton connecting cables are first assembled on a 1.5 mm thick G10 sheet, which serves as insulating separator between the rear connecting planes of each module and the SS bottom plane of the supermodule enclosure. The unit modules have small raised studs at select locations which accurately mate with the aligning holes on the G10 sheet. The alignment is secured by epoxy at the stud positions.

(ii) The entire G10 plane is then lowered into the SS supermodule enclosure, which is clamped to flat (0.5 μm) granite table.

(iii) Connections for cathode HV are made through the SHV connector on the top of the box enclosure forming the supermodule.

(iv) The top shielding plane is positioned after passing all kapton cables through the respective slots.

(v) The edges of the shielding PCB and the boundaries of the kapton con-

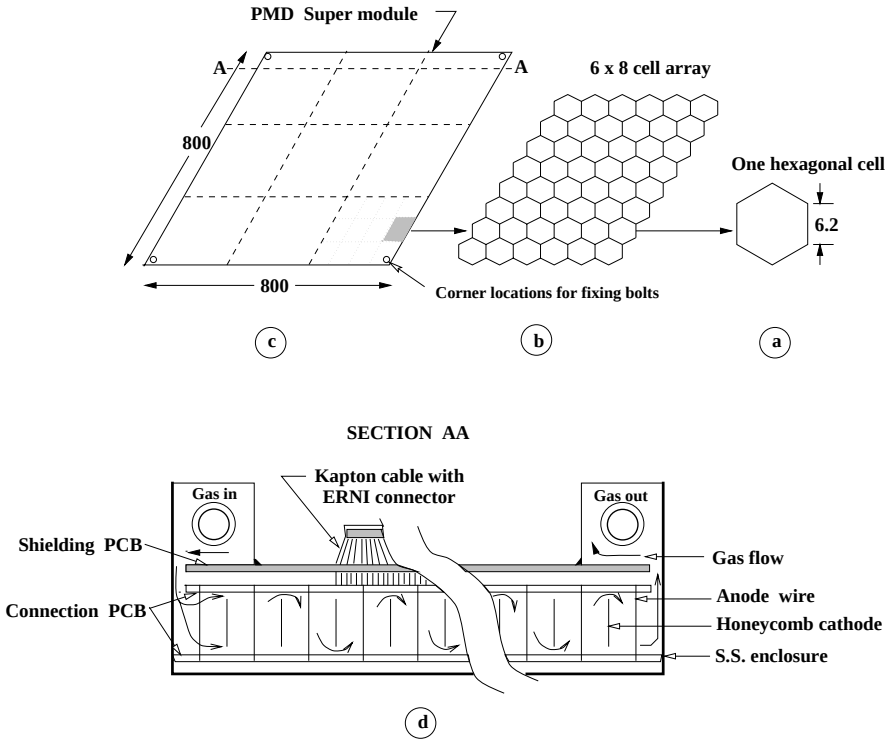

Figure 15: Schematic representation of a Supermodule : (a) unit hexagonal cell, (b) an array of 6 $\times$ 8 cells for one MCM gassiplex card, (c) the Supermodule consisting of 9 unit modules, and (d) section of the supermodule showing electrical and gas connections.

nectors are sealed with RTV sealants.

The assembled supermodule is tested for broken wires using the following scheme : The box module is subjected to ultrasonic vibration using a probe. Suitable field (typically 1 KV/cm) is applied between cathode and anode (wires). The induced signals on the wires are monitored through the ERNI connectors and calibrated to respond, when the wire is broken, by a set of indicator LEDs. Although repair of broken wires is not foreseen, unit modules will be replaced if the number of broken wires becomes more than 5%.

The gas flow impedance for the entire chamber is kept low by incorporating the following schemes :

– small notches are provided at the corners of each cell (as described in the case of the prototype, see Fig. 9) so that gas flows from one cell to another smoothly,

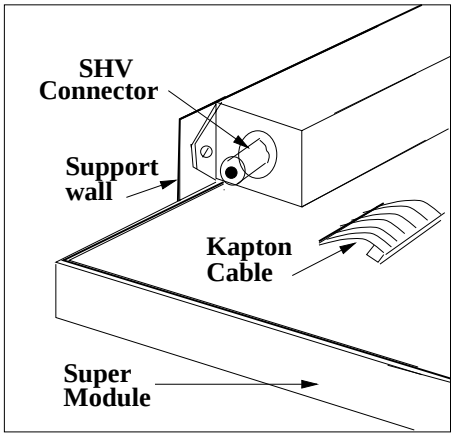

Figure 16: High voltage and gas feed sub-assembly sitting at the top of a supermodule.

– gas is fed through the end connector of the long gas feed channel at the boundary of the supermodule. The feed channel has a number of parallel moulded channels and gas enters simultaneously at several entry points situated at the dead spaces on the edges. It then flows through the notches and exits at the other edge of the SM in a similar fashion. Gas tightness of the enclosure is tested after the assembly with a portable gas leak detector having a sensitivity of 10^{-3} cc of Argon per sec.

4.4 Front-end Electronics

4.4.1 GASSIPLEX readout

The dynamic range of a preshower detector in principle has to be very high, as the cells may receive energy deposition varying from a fraction of a keV (MIP equivalent is 2.7 keV for 8 mm deep cells) to several MeV for high energy photon showers. However electronics chips spanning such a large dynamic range are not available commercially and will be very difficult to design and fabricate.

The readout of the anode signals is proposed to be done using the GASSIPLEX chip developed at CERN. The details can be found in [16]. Efforts are underway to fabricate the chip in India with the same specifications. The new chip based on 0.7 μm technology, will have a dynamic range of 250 fC for negative input from the anode wires of the honeycomb chamber. This should correspond to about 40 MIPs in the preshower mode of operation [14]. It has been estimated that less than 0.1% of the cells will have signal more than this value. For clustering of hits and photon/hadron discrimination, this dynamic range will be

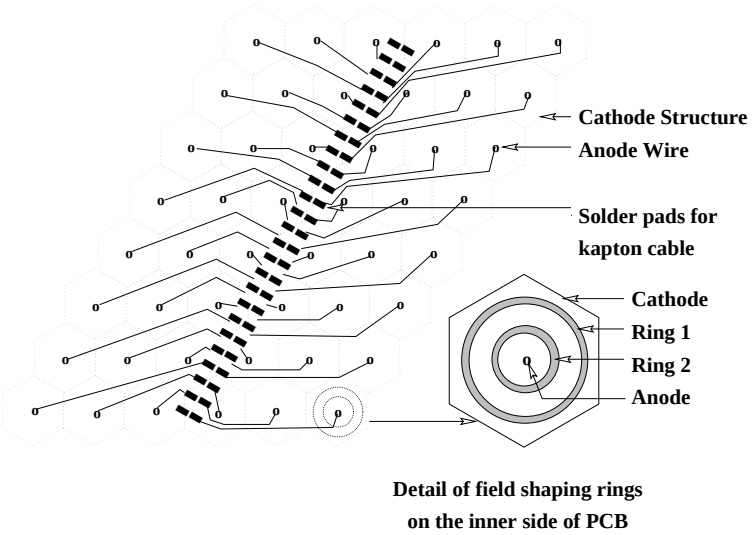

Figure 17: Wiring diagram for one 48-channel unit employing one MCM board.

adequate.

The PMD cells are situated at a minimum distance of 70 cm from the beam at 6 m from the vertex. At this location no radiation problems are foreseen in ALICE environment. Thus there is no extra demand on the front-end electronics from the point of view of radiation hardness.

The unit module has been designed with the aim of using 3-chip MCM boards. Fig. 17 shows the wiring diagram for a 6×8 array of cells using one gassiplex board. We shall closely follow the engineering development of gassiplex readout electronics, including the digital part, undertaken by the ALICE collaboration. The unit module has the option of using a 64-channel (4-chip) board also, in case it is decided to use such boards. This uniformity in design with other ALICE sub-detectors using gassiplex electronics will help in easier integration of the data acquisition of the PMD with the main system. This will also help the PMD to take data in conjunction with the dimuon spectrometer and other high rate detectors in ALICE.

4.4.2 Chip tests

Considering that chips will be fabricated in India, a comprehensive setup for testing and assembly of chips has been developed at VECC in collaboration with CERN for 3-chip boards [17]. The board GB1, shown in Fig. 18, has three gas-

siplex chips G1, G2 and G3. The control signals and low voltages are connected in a specific way through the pin-rows B1 and B2. Since gassiplex is operated at $\pm$3.5 V and GND, all the fast NIM control signals (clock, clear, T/H) have to be shifted to levels required for gassiplex operation. This is accomplished by a level shifter LS on the test board. Repeaters REP1 and REP2 are used to duplicate the low voltages and control signals to allow parallel operation of many chips. The test pulses can be sent to all the channels through a calibrated capacitance via a common test input line.

An indigenously developed NIM module (VECC CONTROL UNIT) generates the fast NIM control signals (clear, clock, T/H) on being provided a trigger input from a tail pulse generator. The trigger output of the tail pulse generator should be connected to the oscilloscope and programmable pulse generator keeping it in Ext/Sc mode. The positive output of this can be used as test signal. The number of clocks can be selected by means of front panel switches in Hex Code on the control unit. The maximum number of clocks that can be preset is 256, i.e., 16 chips can be daisy-chained with the present unit.

With this setup, one can test the chip for power consumption, full functionality of gassiplex operation, clock out, output d.c. level and noise measurement, pedestal spread, sensitivity, linearity, peaking time measurement with base resistance, variation of d.c. level measurement with temperature, dynamic range etc.

4.4.3 Low voltage system

The operating voltage for gassiplex is $\pm$ 3.5 V. For one UM (576 channels) 12 MCM boards having 3 gassiplex chips each will be required. The chips used in a unit module will be supplied separately by a pair of voltage regulators mounted on the power and slow control board. All the boards used in a supermodule (108 MCM boards) will in turn be fed by a main double power supply. The double power supply is necessary to ensure simultaneous availability of both polarities at power-on.

The voltage regulators for each UM have to be able to sustain 4.5 watts each. A protection circuit will be used for detecting overcurrent in case of latch up. The supplies of the modules concerned by this latch up will be switched off on overcurrent. Two other power supplies will be needed for digital electronics.

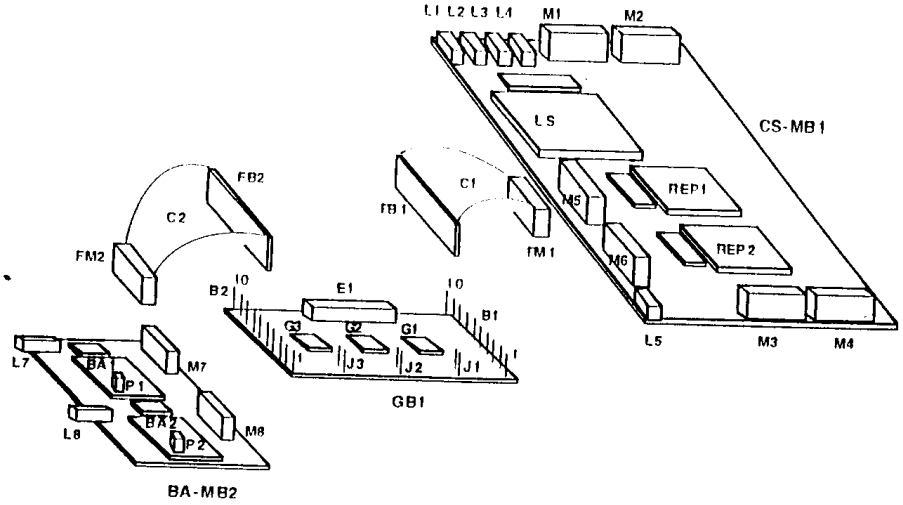

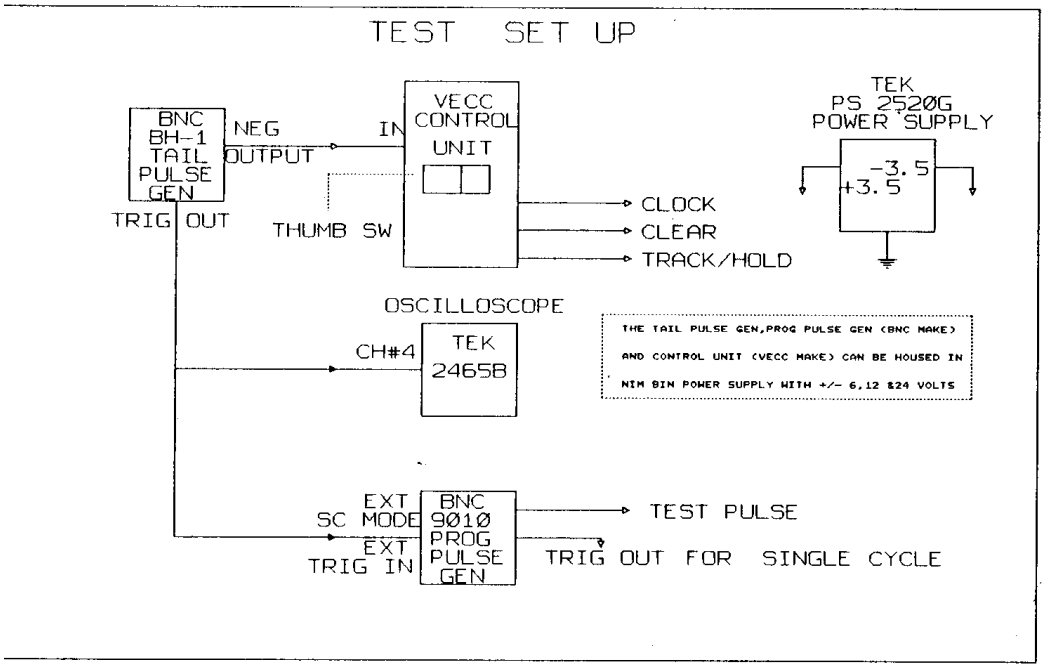

Figure 18: Block diagram of the test setup for gassiplex chips

4.5 Support Structure and Converter

The support structure for the PMD is designed to handle a total weight of 6000 kg and will be fabricated from exclusively non-magnetic components. A set of stainless steel (SS) I-beams, fitted with hydraulic devices, are fixed on the door of the ALICE magnet to provide X- and Z- movements, as shown in Fig. 19. The entire detector is divided into two halves, which are identical in all respects and can move independently in both directions. A 6 mm thick SS plate, used separately for each half, forms the main support for the lead converter plates and the detector SMs.

Lead converter plates will be machined in the form of rhombuses of side 20 cm so that the weight of each piece is around 8 kg and easy to handle during installation. These will be fixed onto the SS support plate by two screws each. There will be thru holes in lead plates at the positions where SM will be fixed with the support plate. The SMs for the CPV and the PMD (first preshower plane) will be mounted back-to-back on one support plate. There will be a separate support plate for the second preshower plane.

5 Physics Performance

The physics performance presented here is based on central Pb + Pb events from the VENUS event generator and GEANT simulation.

5.1 Low p_T Selection

5.1.1 p_T acceptance

The p_T acceptance of the PMD for photons is shown in Fig. 20. The upper curve represents the fraction of photon clusters (N^{γ}_{cls}) remaining after applying NN threshold for hadron discrimination and the lower curve represents the same quantity obtained after applying a 3 MIP-threshold on cluster signal for hadron rejection [18]. It is clear that the PMD is capable of detecting very low p_T particles, down to 20 MeV/c. The NN method of hadron discrimination retains much larger fraction of low p_T particles, about 25% higher than cluster threshold method for $p_T < 150$ MeV/c.

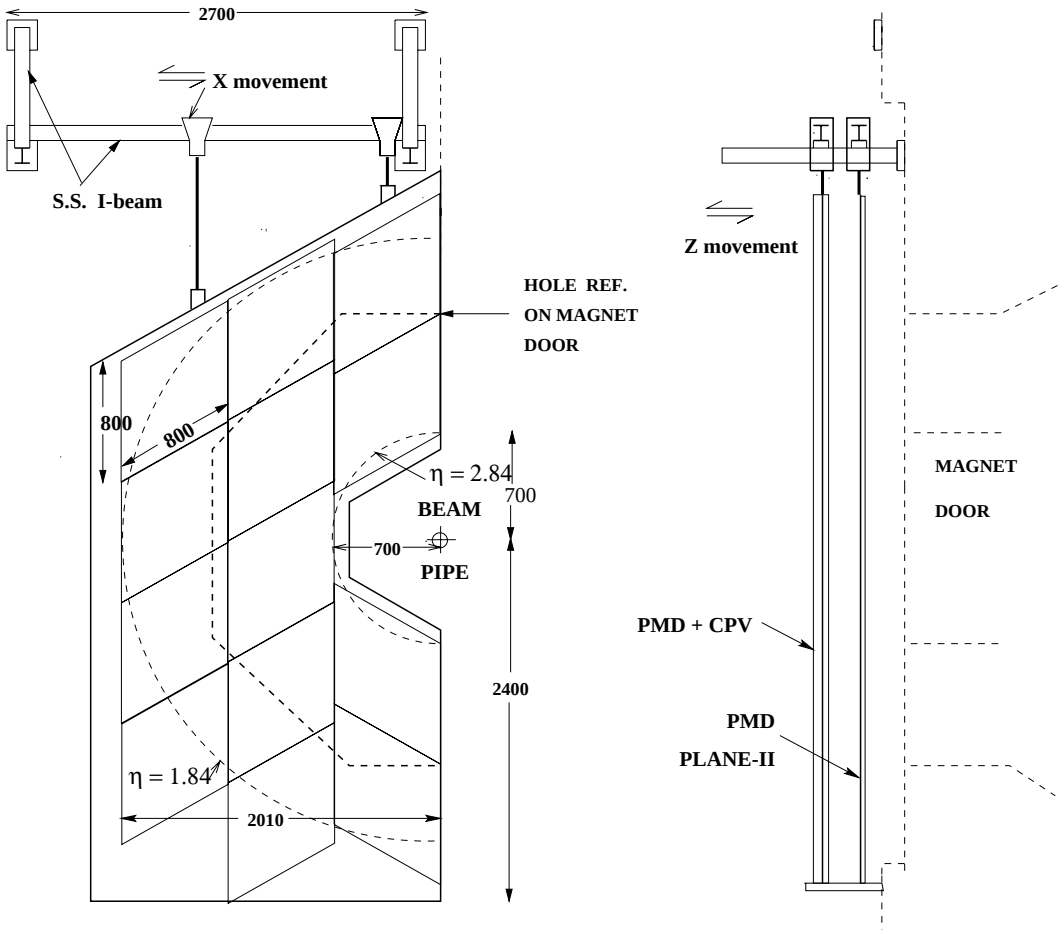

Figure 19: Hanging mechanism of the PMD, along with section of half the detector containing 13 supermodules. The central hole is 70 cm in radius.

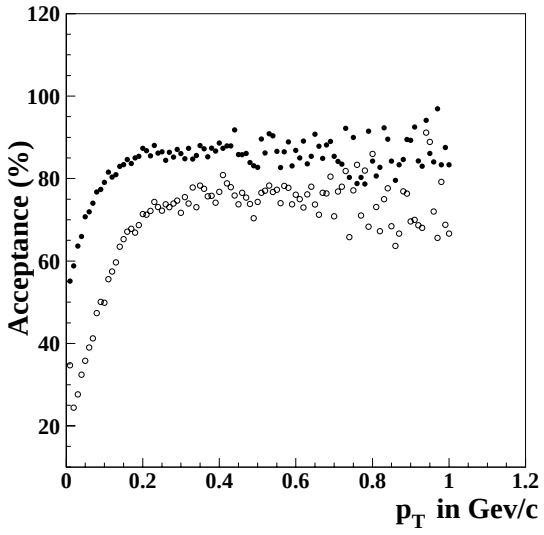

Figure 20: p_T acceptance of the PMD : open circles represent hadron rejection by threshold on cluster signal without the CPV and filled circles denote neural network method using the CPV.

5.1.2 Enrichment of low p_T photon sample

One of the important recent propositions of the QGP signatures is related to the existence of tricritical point [19] which predicts non-thermal enhancement of soft pion spectrum at $p_T < m_\pi$. It is also predicted that the event-by-event fluctuation in the multiplicity and distribution of soft pions will increase. The pions produced in DCC are also predicted to have predominantly low p_T. The observation of these effects requires careful selection of low p_T particles, which will be possible in the mid-rapidity region of ALICE using ITS/TPC for charged particles and to some extent using PHOS for photons.

While the PMD cannot measure p_T of individual photons, the variable p_T^{PMD} calculated using the preshower signal ΔE can be employed to select a sample of photons which are enriched in given low p_T classes. Because of the approximate proportionality of the preshower signal ΔE with the incident photon energy, p_T^{PMD} $(=\Delta E.sin\theta$, where θ is the angle at which a preshower cluster appears) shows a weak correlation with the p_T of the incident photon [7].

The results of suitable cuts on p_T^{PMD} ($p_T^{PMD} < p_T^{PMD}(lim)$, a pre-selected value obtained from p_T^{PMD} spectra) are shown in Fig. 21 (a). S denotes the fraction of signal photons (having p_T below some desired value, 150 MeV/c in

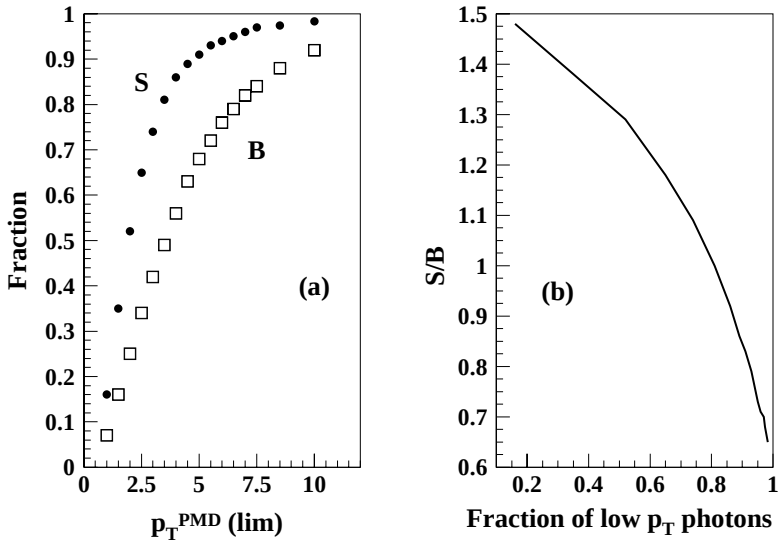

Figure 21: (a) Fraction of signal photons (with $p_T \leq 150$ MeV/c, solid circles) and fraction of background photons (with $p_T > 150$ MeV/c, open squares) as a function of $p_T^{PMD}(lim)$, (b) Signal-to-background ratio for selecting photons with $p_T < 150$ MeV/c as a function of fraction of low p_T photons.

the present case) and B denotes the fraction of background photons (having p_T outside the desired range) in a given sample. It is found that the reduction in background photons is always larger than the corresponding reduction in signal photons. Maximum difference arises around p_T^{PMD} values such that for a loss of $\sim$20% in S, the reduction in B is more than 50%. Thus the signal-to-background ratio S/B continuously increases as one moves towards smaller p_T^{PMD} cuts, as shown in Fig. 21(b). S/B is the least for no selection case, where all the signal and background photons are present in the sample. Near the edge, it increases sharply even for smaller reduction in the fraction of signal photons. Thus, even though a pure sample of signal photons can not be selected using the preshower detector, the photon sample can be easily enriched in given low p_T species. Although S/B goes on increasing for smaller cuts on p_T^{PMD}, the loss of useful signal particles may suppress the physics, and one has to make a suitable compromise. If there are physical phenomena associated with the production of low p_T photons in the phase space region covered by the PMD, characteristic changes in experimental observables can be distinguished by applying cuts on the p_T^{PMD} values.

5.2 Disoriented Chiral Condensates

Disoriented chiral condensates (DCC) have been predicted to form in case of high energy collisions when the chiral symmetry is restored at high temperatures and densities. As the matter cools and expands, the vacuum could relax into a state that has an orientation different from the normal vacuum. This could result in an excess of low momentum pions in a single direction in isospin space, leading to formation of localized DCC domains [20, 21, 22, 23, 24]. It has been estimated [20] that the neutral pion fraction, f, of pions from the DCC domain, follows the probability distribution:

$$P(f) = \frac{1}{2\sqrt{f}} \qquad \text{where} \quad f = N_{\pi^0}/N_{\pi} \tag{4}$$

The formation and decay of DCC domains give rise to isospin fluctuations of pions, where the neutral pion fraction can deviate significantly from 1/3. This would lead to event-by-event fluctuations in the number of charged particles and photons in a given phase space, since majority of the photons originate from π^0 decay and contents of the charged particles are mostly charged pions. The most abnormal charge-to-neutral fluctuation observed so far has been Centauro and Anti-centauro events seen in cosmic ray experiments [25].

The experimental observation of DCC depends on various factors, such as the probability of occurrence of DCC in a reaction, number of possible DCC domains in an event, size of the domains, number of pions emitted from the domains and the interaction of the DCC pions with rest of system, about which not much has been known theoretically [26, 27, 28]. Only a few attempts have been made to look for DCC in laboratory experiments [29, 30].

Searching for the occurrence of DCC can be made either by studying a large ensemble of events and looking for some deviation in a distribution characterizing the DCC. Such an effort has already been tried in the case of WA98 experiment [30]. In the same way one can search for localized domains as described in detail below. A different approach is to look for abnormal effects on an event-by-event basis.

5.2.1 Search for localized domains

Using wavelet analysis [31] applied to $(\eta - \phi)$ distribution of photons and charged particles measured using suitable multiplicity detectors in a common part of phase space, one can generate a set of wavelet or father function coefficients (FFCs) at different length scales (j). The FFC distribution of normal (or generic) events

having no DCC is gaussian at all scales, whereas the presence of DCC broadens these distributions and changes their shapes. The amount of broadening depends on various factors associated with DCC domains and can be quantified by the rms deviations (ξ) of the distributions. One can then compare different distributions by the strength parameter defined as [32] :

$$str = \frac{\sqrt{(\xi^2_{\rm DCC} - \xi^2_{\rm normal})}}{\xi_{\rm normal}} \tag{5}$$

where $\xi_{\rm normal}$ is the rms deviation for normal events and $\xi_{\rm DCC}$ is the rms deviation for a sample of events having built-in DCC domains. The method has been developed at the SPS energy [32] using VENUS events as normal events. DCC type events have been generated by the following assumptions :

- (1) Since pions from DCC domains are of low p_T, we assume that out of all the pions present within the chosen domain in a VENUS event, only low p_T pions may be of DCC origin. The identity of the pions with p_T <300 MeV/c in VENUS events are interchanged pairwise according to the DCC probability distribution as given by eqn. 4 to produce new events.

- (2) A number of low p_T pions, generated according to DCC probability given in eqn. 4, are added within the chosen domain on top of the existing pions from VENUS.

For assumption (2), the number of additional pions depends on the size of the DCC domain and the energy density of the domain. For this case, the number of DCC pions added are kept fixed irrespective of the size of the DCC domain.

Fig. 22 shows the simulation results on the strength contours at the SPS energy for different domain sizes and probabilities of occurrence of DCC type events using the sample function

$$f' = \frac{N_\gamma}{N_\gamma + N_{\rm ch}} \tag{6}$$

where N_γ and $N_{\rm ch}$ are the multiplicities of photons and charged particles, respectively. The full azimuth was divided into 32 bins for generating the FFCs corresponding to scale j_{max}=5. The top part of the figure shows the strength contours at two scales $j = 1$ and $j = 2$ for assumption (1) and the bottom part shows the same for assumption (2). The solid and dashed contours in the bottom part are drawn corresponding to 100 and 60 additional DCC pions, respectively.

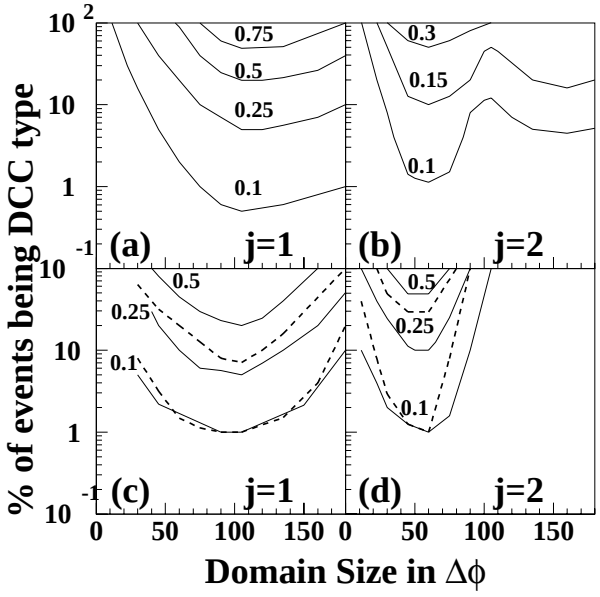

Figure 22: Strength contours for j=1 and j=2 for two assumptions about the DCC events

The lowest contour corresponds to a strength value below which the method is not sensitive either to the change of domain size or to the probability of occurrence of DCC, i.e., no distinction can be made between normal events and DCC type of events. Using the rms deviation of the FFC distribution of normal events, and the statistical error associated with it, this limiting strength value is estimated to be 0.1. The figure indicates that the method is sensitive to very low values of the probability of occurrence of DCC events ($\sim 1\%$), for domain sizes of 90^o and above in case of $j = 1$ and $40-60^o$ for $j = 2$. From the values of *str* at different j's, one may draw inference about the size and probability of occurrence of a possible DCC domain.

Preliminary analyses of WA98 data indicate that the strength value is slightly above the limiting strength at the scales studied. This suggests that detectable DCC effect may be present in the data. However, more rigorous analyses, in progress, will be required to confirm/deny this.

Using the PMD and the FMD in ALICE, one can continue similar analyses for searching localized DCC domains. Because of very high multiplicity one can go up in scale without encountering large bin-to-bin statistical fluctuations. This is expected to enhance the sensitivity of the method.

5.2.2 Event-by-event method

The probability of occurrence of DCC events may be even smaller than the sensitivity of the global technique described in the previous section. In such a situation it becomes necessary to develop analysis tools which are more sensitive and can be used on event-by-event basis to study isospin fluctuations. The power spectrum technique has been recently developed for the study of event-by-event fluctuation in pseudorapidity distributions [33]. The method is quite powerful and can be applied to study event-by-event fluctuations in the azimuthal distribution of N_γ/N_{ch} over limited ϕ-regions typical of DCC domains.

The ratio $f_1 = N_{\gamma-like}/N_{ch}$ is computed for a window of 60^o in azimuth starting from any selected ϕ-value. The window is then moved by 6^o and f_1 is computed again for a window of the same size. In this way one gets a set of f_1 values for one event, to construct a $df_1/d\phi$ distribution. The power spectrum of this distribution is then obtained in a manner similar to that obtained for the pseudo-rapidity distribution [33]. For finding exotic events, an average power spectrum for VENUS events is calculated and thresholds determined so that normal VENUS events show very small statistical fluctuation above the selected threshold.

The method is under development, but has been tested on the WA98 data set. Fig. 23 shows the event display of PMD and SPMD hits in a particular event selected as "exotic" using the above method. The event has a large region devoid of charged particle hits. The origin of such a large asymmetry is under investigation. The present example is only given to demonstrate the power of the method and also the capability of the PMD.

Using $dN/d\phi$ distribution over limited ϕ-windows, one can use the power spectrum method to study minijets.

5.3 Azimuthal Anisotropy and Flow

Observation of collective flow in nuclear collisions is crucial for our understanding of the hydrodynamical description of the evolution of the collisions and the process of thermalization. Collective flow manifests in altered event shapes which can be studied by measuring the spatial and momentum distribution of produced particles.

An obvious advantage in studying event shapes using photons is that the transverse distribution of the photons, unlike those of charged particles, are not

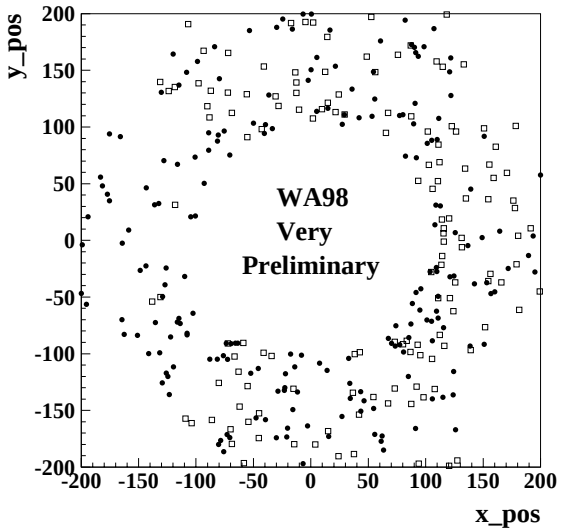

Figure 23: The x-y display of an abnormal event in WA98 experiment picked up using the power spectrum method applied to azimuthal distribution of $N_{\gamma-like}/N_{ch}$. Solid circles are photon hits and open squares are charged particle hits.

affected by the final state Coulomb effects.

Among various techniques to determine anisotropies in the transverse plane, the Fourier expansion of the azimuthal distribution has been used extensively [34]. This method can also be applied to data where only the spatial distribution of produced particles is measured without the knowledge of their momenta.

The azimuthal anisotropy of photons was studied using the very first PMD in the WA93 experiment [3] following the analysis method given in Ref. [35]. In this study the photon hits on the PMD in S + Au interactions at 200 A GeV were subdivided into two pseudorapidity regions within the acceptance of the detector. These constituted two sub-events. Correlations between the event planes determined by the two sub-events allowed one to study the azimuthal anisotropy and hence the elliptic flow. The results are shown in Fig. 24 indicating elliptic flow of $\sim$5% in semi-central collisions. The background effects contributing to flow are within 2%, except for the extreme peripheral case.

To investigate the effectiveness of the ALICE PMD in the study of azimuthal anisotropy and flow, a simple parametrization of HIJING1.31 events in the η range 0-5 has been used for fast simulation [36]. Such a parameterization results in the charged particle multiplicity of about 3800 in the range $1.8 \leq \eta \leq 2.8$. The centrality has been varied by changing the multiplicity M of charged particles,

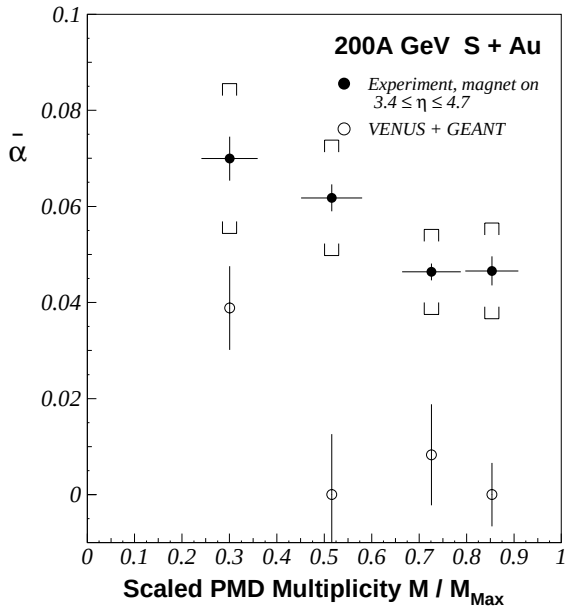

Figure 24: True azimuthal anisotropy $\overline{\alpha}$ as a function of PMD multiplicity in S + Au collisions at the SPS energy.

the multiplicity distribution being assumed to be gaussian with $\sigma = 2\sqrt{M}$. We assume that the neutral pions are described by the same kinematic distributions as those of the charged pions. The decay of the neutral pion within (outside) the acceptance region often results in a photon falling outside (within) the region. Therefore neutral pions were generated within the η-range $\pm$ 1.5 units on both sides of the PMD acceptance.

5.3.1 Directed flow

The sensitivity of the PMD to directed flow has been studied by generating azimuthal angles according to the probability distribution

$$r(\phi) = \frac{1}{2\pi}\left(1 + 2v_1 cos(\phi - \psi_R)\right) \tag{7}$$

where ψ_R is chosen randomly. v_1 characterizes in-built anisotropy. This method has the advantage of incorporating the fluctuation in the event plane determination due to finite particle multiplicity.

The decay photons falling within the PMD acceptance, along with charged particles, are used for further analysis to estimate v_1 using Fourier coefficient

TABLE VI (a)
Comparison of directed flow observable using charged particles and photons.

Mult.	$\pi^{\pm}$		γ	
	v_1	RCF	v_1	RCF
200	0.050	0.555	0.057	0.581
1000	0.050	0.875	0.041	0.810
2000	0.050	0.948	0.041	0.906
4000	0.050	0.972	0.041	0.950

method. The resolution correction factor (RCF) for the event plane determination has been obtained by dividing the event into two subevents, and counting the fraction of events in the data sample yielding an angle between the subevents more than $\pi/2$ [34].

Charged particles have been generated for M = 200, 1000, 2000 and 4000 corresponding to semi-central collisions. The azimuthal angles have been generated to give them 5 % flow (v_1=0.05). For all data samples, the technique is able to estimate the magnitude of flow correctly. The distribution of v_1 for all the events varies with multiplicity, it being widest for the smallest multiplicity, causing a greater statistical error in v_1 for smaller multiplicities. The resolution of the event plane determination also changes with multiplicity, and is best for higher multiplicities. For a perfect determination, the RCF is expected to be unity.

Table VI (a) gives the value of the estimated flow, and the RCF, both for charged particles and photons.

The process of decay also dilutes the observed signal of flow. This is because the v_1 value obtained for small multiplicity includes the actual contribution of flow of π^0, and the correlation due to decay, resulting in an overestimate of the v_1 value. The effect of correlation due to decay becomes negligible at higher multiplicities, where the estimated values of v_1 are lower.

The sensitivity of the PMD to detect small amount of directed flow has been studied by generating events with M = 2000 and v_1= 0.025, 0.05 and 0.1 and analysing both photon and charged particle distributions. The results are shown in Fig. 25. It is found that the effect observed with photons is always a little lower compared to charged particles, but the effect persists even at the smallest value v_1=0.025.

The effect of photon counting efficiency and purity on the observable asym-

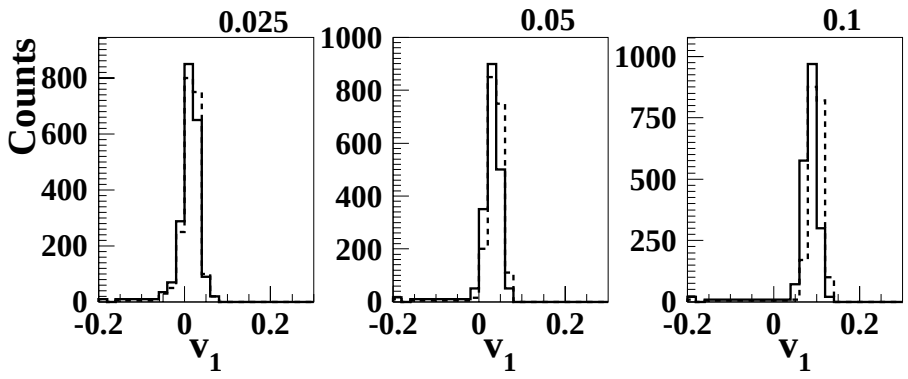

Figure 25: Residual directed flow for various input anisotropies $v_1 = 0.025$, 0.05, and 0.01 as indicated at the top of the frames, for $M = 2000$. Continuous and dashed lines denote the estimated values of v_1 using photons and pions respectively.

metry has also been studied. The efficiency does not seem to have any effect other than that due to decreasing multiplicity. The estimated values of v_1 do not show any dependence on the amount of impurity. The resolution correction factor increases with increasing impurity, showing that the effect is only due to increase in the total multiplicity detected.

5.3.2 Elliptic flow

The simulation has also been performed for investigating the sensitivity of the PMD to elliptic flow in a manner similar to that described for directed flow. Table VI (b) gives the values of the estimated elliptic flow (v_2) and the RCF for various multiplicities.

The results indicate that the magnitude of the estimated value of v_2 using charged particles is equal to the initial anisotropy given to the particle distribution. However, the estimated value of v_2 using photons is substantially lower than the initial anisotropy, the reason being dilution of flow due to the decay of π^0. It is also seen that the decay dilutes the elliptic flow more than it dilutes the directed flow. At low multiplicity the observed dilution due to decay is partially offset by the correlation due to energy-momentum conservation, which is known to contribute to observed flow. For small value of $v_2 = 0.025$ given initially, the estimated value may be barely above the background contributions.

TABLE VI (b)
Comparison of elliptic flow observable using charged particles and photons. For the first 4 rows, the input value of v_2 was 0.05, and for the last 2 rows it was 0.025 and 0.1 respectively.

Mult.	$\pi^{\pm}$		γ	
	v_2	RCF	v_2	RCF
200	0.050	0.502	0.041	0.434
1000	0.050	0.870	0.033	0.699
2000	0.050	0.942	0.032	0.833
4000	0.050	0.972	0.031	0.894
2000	0.025	0.765	0.018	0.588
2000	0.10	0.982	0.062	0.960

5.4 Event-by-Event Studies

5.4.1 Fluctuation in N_γ/N_{ch}

The fluctuation in N_γ/N_{ch} is shown in Fig. 26. The top part shows raw VENUS values having a sigma of 2.3%, the bottom part shows the plot of $N_{\gamma-like}/N_{ch}$, having a sigma of 2.6% after full GEANT simulation of the PMD. Although poor statistics prevents us from drawing a conclusion about the shape of the distribution, it is found in practice to have perfect gaussian shape, as can be seen from the experimental distribution of a related observable, D_z, which measures the disperson of the correlation between N_γ and N_{ch} [30]. The D_z distribution derived from measurements using the PMD and the SPMD detectors in WA98 experiment is shown in Fig. 27. It is remarkable to note that the experimental data follow a gaussian distribution over more than four orders of magnitude.

The above gaussian distributions suggest that the PMD data can be used to study event-by-event fluctuations. For estimating the sensitivity of the ALICE PMD to event-by-event fluctuation in N_γ/N_{ch} a simple investigation has been done using gaussian–distributed random numbers having the fluctuations as described above [4]. With these parameters we calculate $N_{\gamma-like}$. Efficiency for N_{ch} is assumed to be 100%. The mean of the resulting $N_{\gamma-like}/N_{ch}$ distribution is 0.88 and the width (σ) is 3%.

We generate another set of events by adding a certain percentage of photons to the above number, keeping the number of charged particles fixed. Fluctuations in the input number of photons, efficiency and background are increased so that the resulting distribution has width (σ) $\sim$ 5%.

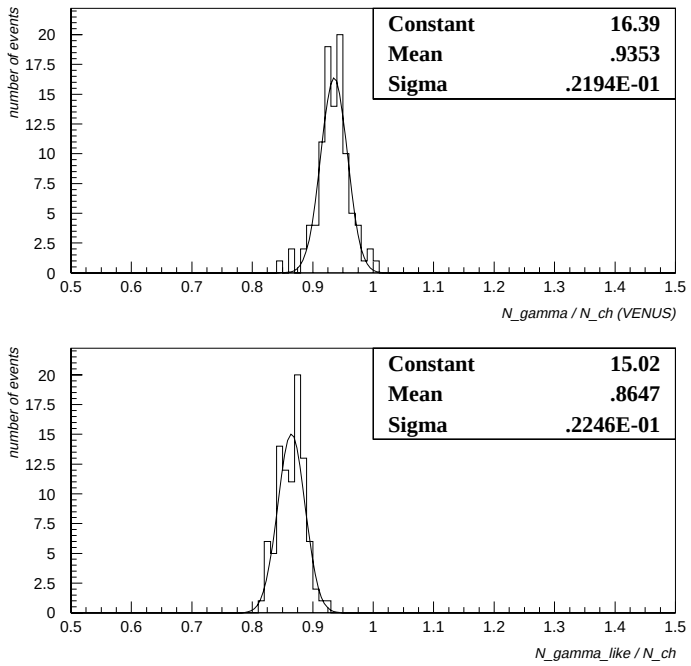

Figure 26: Top : Ratio N_γ/N_{ch} from VENUS event generator in the pseudo-rapidity range $2.3 \leq \eta \leq 3.3$, Bottom : The ratio $N_{\gamma-like}/N_{ch}$ of the γ-like clusters measured on the preshower part and the charged particles in the charged particle veto.

By mixing a small percentage of the photon-enhanced events with a large set of normal events and studying the tail region of the resulting distribution, we have computed the efficiency of filtering the enhanced events for various percentages (5,10,20) of photon enhancement in 0.1%, 0.5% and 1% of the normal events.

The sensitivity is studied by the efficiency of selection for cuts on the tail region which gives at least 90% purity of the signal (photon–enhanced sample of events) which corresponds to S/B > 9 (where S is the number of enhanced events found in a selected part of the tail, and B is the number of background or normal events in that part of the tail). For reliable selection of exotic events as required for detailed event-by-event studies, the criterion of high purity is much more important than that of high efficiency. If the reliability of selection is high, i.e., if the sample in the tail region is almost pure, then the exotic events can be studied by increasing the statistics.

Fig. 28 summarizes the results for the various cases studied. Cases 1,2,3 correspond respectively to 1%, 0.5% and 0.1% of the events being photon–enhanced type and with fluctuations deduced from the GEANT simulation of the PMD.

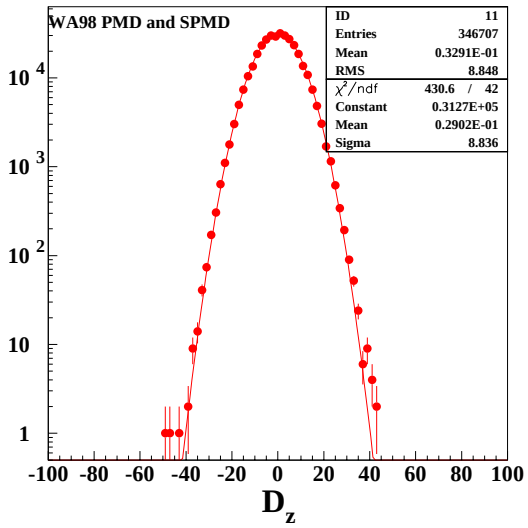

Figure 27: D_z distribution for correlation between N_γ and N_{ch} measured using the PMD and the SPMD in the WA98 experiment. Each event was divided into four quadrants and D_z determined for each quadrant.

Case 4 represents the results like Case 1 where fluctuations were arbitrarily increased so that the width (σ) of N_γ/N_{ch} in the normal sample of events was 5% and that for the photon–enhanced sample was 7%. This will correspond to a case of reduced multiplicity $N_\gamma, N_{ch} < 500$, which might be encountered either due to different pseudorapidity distribution or because of reduced phase space in which one is looking for interesting isospin fluctuations (e.g., localized DCC domains). It is evident that with sufficient statistics isospin fluctuations down to 10% of the normal value can be easily studied using the PMD in ALICE.

5.4.2 Fluctuation in pseudorapidity distribution

The event-by-event fluctuation in pseudorapidity distribution has been studied using the power spectrum method [33, 37, 38]. Using artificially injected non-statistical fluctuations, it has been demonstrated that a reference average power spectrum can be generated which is almost independent of the level of admixture of non-statistical fluctuation. This technique can be directly applied to the experimental data.

Small amounts of non-statistical fluctuation can be reliably detected even with a detector having finite coverage like the PMD. Using stricter criterion such that statistical noise is less than a percent, the efficiency of selection of events

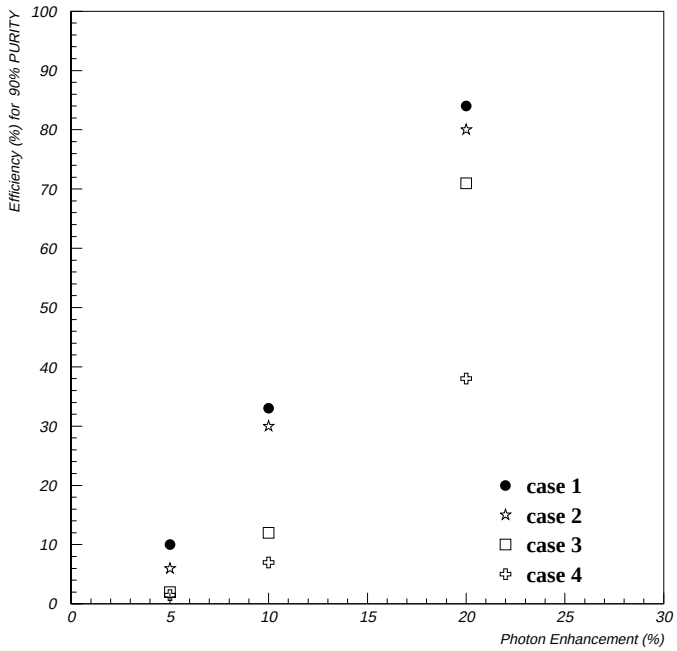

Figure 28: Efficiency of selection of the signal with greater than 90% purity for various values of percent photon enhancement. Cases 1,2,3 correspond respectively to 1%, 0.5% and 0.1% of the events being photon–enhanced type with fluctuations given by the GEANT simulation. Case 4 represents 1% of the events being photon–enhanced type, with fluctuations increased.

having certain non-statistical fluctuation (called exotic events) characterized by spike in a η-bin of size $\delta\eta$=0.1, as shown in Fig. 29, is given in Table VII for various values of P and R. P denotes the spike strength, which is a small fraction of the multiplicity, added in a η-bin. R denotes the percentage of total events which are of exotic nature.

5.5 Estimation of E_T^{em}

The PMD can be used to provide an estimate of the e.m. transverse energy E_T^{em} using the measured preshower signals. Although there are large fluctuations in the energy deposited by individual photons in a preshower detector, the fluctuation substantially reduces when the summed energies of a large number of particles are considered. For the preshower PMD, a working estimate of E_T^{em} can be given by the relation [5]

$$E_T^{PMD} = \sum_i \Delta E_i . \sin\theta_i \qquad (8)$$

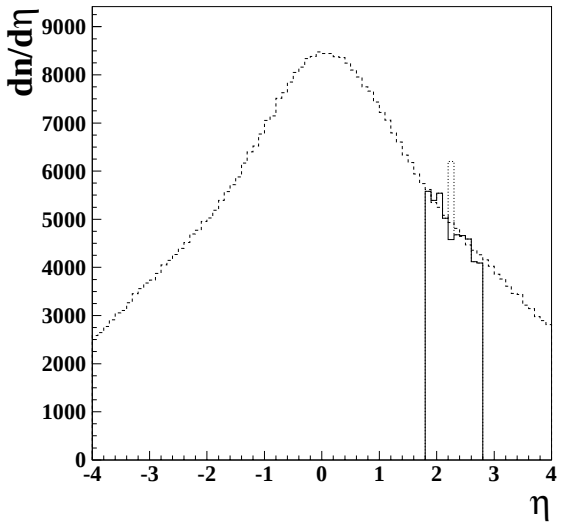

Figure 29: Pseudo-rapidity distribution of photons : dashed line denotes the average for VENUS events, solid line denotes one VENUS event in the PMD acceptance and dotted line shows a spike in one η-bin as described in text.

TABLE VII

The efficiency (on the left column) and impurity (on the right column) for identifying exotic events at the LHC energy for different values of P and R. The numbers have been rounded to the nearest integer.

	large coverage (-3,3)						PMD coverage (1.8-2.8)					
R$\downarrow$ \ $P \rightarrow$	0.35		0.5		1		0.35		0.5		1	
1	37	33	93	13	100	12	20	50	73	28	100	33
5	35	11	89	5	100	4	25	13	86	4	82	4
10	31	7	90	2	100	3	28	6	87	2	83	3
20	27	4	89	1	100	1	33	2	84	1	87	2
30	33	2	90	1	100	1	23	2	82	1	84	1

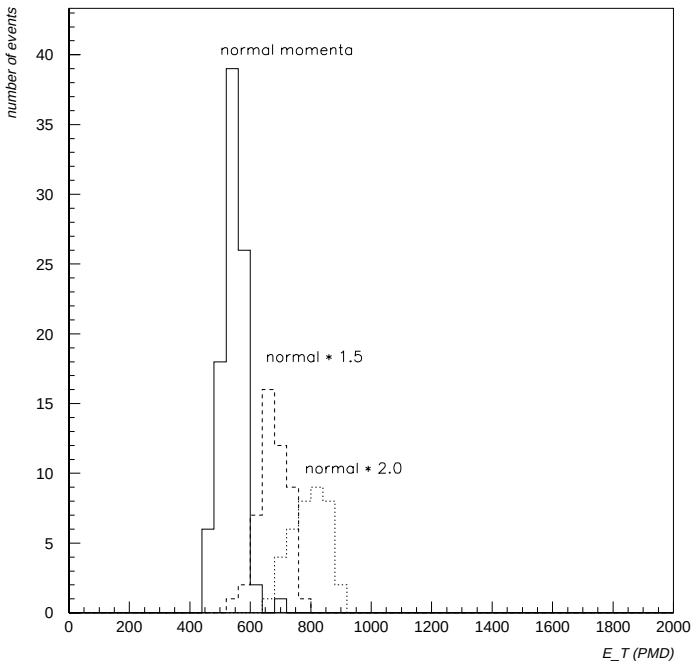

Figure 30: Histograms of E_T^{PMD} for the three cases as indicated. Solid curve is for normal venus events, dashed curve for venus events with momenta increased by 50% and the dotted curve for VENUS events with momenta increased by 100%. The x-axis scale is in arb. units.

where θ_i is the angle at which the i^{th} γ-like cluster appears, ΔE_i is the energy deposited in the sensitive volume of the PMD by the i^{th} cluster, and the sum runs over all the observed γ-like clusters. The preshower signal ΔE_i is approximately proportional to the incident photon energy as the number of shower electrons increases almost linearly with photon energy upto about 10 GeV [15]. We denote E_T^{em} measured by the PMD as E_T^{PMD} to distinguish it from the calorimetric measurement of E_T^{em}. E_T^{PMD} is found to be a small but constant fraction of E_T^{em} [1].

To study the sensitivity of the preshower signal to variations in the E_T in the event, we have modified VENUS events by multiplying the momenta of all the particles by 1.5 and 2, thus increasing the E_T by 50% and 100% respectively. The results obtained for the E_T^{PMD} are shown in Fig. 30 for the three cases. The solid histogram shows the E_T^{PMD} values for normal VENUS events without any modification, the other two respectively show the E_T^{PMD} values for the case of modified events with increased E_T. The values in the three cases are 540 $\pm$ 35, 680 $\pm$ 45 and 800 $\pm$ 55 respectively. The widths of the histograms denoting event–to-event fluctuation are found to be around 6.5 % in all the cases [4].

As the E_T^{PMD} is estimated using the signal strengths of γ-like clusters, the value is not purely electromagnetic, it has some contamination from hadronic and other backgrounds. It has been estimated that the contribution of the contaminants to the estimated total E_T^{PMD} is 23%, of the same order as the contamination for photons in the sample.

An improvement in the event-by-event fluctuation of measured E_T^{PMD} is possible by adding a second sampling layer of the detector, with rather coarse granularity, behind the preshower layer with 3-4 X_0 thick converter. The cost of this layer is expected to be not more than 10% of the entire cost, mainly comprising of the cost of the detector hardware. Preliminary simulation indicates that the width (σ) of the E_T^{PMD} distribution reduces by a factor of 2 by the use of the second plane. The ratio E_T^{PMD}/E_T^{em} also increases by about a factor of 2.5. In this case it may be possible to study the pseudo-rapidity dependence of E_T^{PMD} [9] and also flow using this variable. More simulation will be carried out to investigate this possibility.

6 Implementation

6.1 R&D and Tests

6.1.1 Cellular honeycomb chamber

The results on prototype tests described in sec. 3 suggest that the honeycomb cellular chamber design is a workable solution for both the PMD and the CPV. Further R&D on the chamber design using guard rings will be carried out. The gas thickness needs to be optimized to values close to that described in the simulation section. For the development of the chamber beam tests will be carried out at the PS.

Techniques for applying graphite paint to the plastic honeycomb will be investigated. Prototype chambers will also be subjected to mechanical and heat stress to learn about problems which may arise in transportation and installation. Modifications in the chamber design to further improve the gas conductance will be tried. Jigs and fixtures for fabrication of the UMs and for assembly of the SMs will be designed and tested. Soldering techniques for anode wire tips will be perfected so that a semi-automatic process can be adopted for fabrication.

The application of hadron discrimination algorithm is based on good knowl-

edge of the shower profile of photons at various energies. It is required to have an exhaustive data set for electron beams at various energies from the lowest values (say 0.5 GeV) to 50 GeV to be able to investigate the detector characteristics and deduce suitable transfer functions as described in [6]. For this beam tests will also be carried out at the SPS energies.

6.1.2 Garfield simulation

Use of guard rings has been proposed as one of the techniques for improving the efficiency of the honeycomb chamber near the edges. For this a detailed simulation using GARFIELD code [39] has been undertaken. The hexagonal cell used in this simulation has 6.2 mm side, giving cell area of 1 sq.cm., and 10 mm depth. Preliminary results on the potential distribution for a hexagonal cell without and with two guard rings are shown in Fig. 31 and 32 respectively. A comparison of these two equipotential lines reveals that the use of guard rings greatly helps in orienting the equipotential lines parallel to the anode wire. Fig. 33 shows the fraction of electron drift lines falling on the anode. The dashed curve shows the results for a cell without guard rings. The solid curve shows the results when two rings, each 0.5 mm wide, were placed at 1.7 mm and 3.8 mm from anode. The cathode was kept at -2500 V and the voltage applied to the rings correspond to a logarithmic radial dependence. There is a remarkable improvement in the field distribution leading to increase in the fraction of primary ionization tracks collecting at the anode. This will certainly improve the uniformity in the efficiency of the chamber within a cell. Further optimization is in progress by varying the voltages on the rings and the width and location of the rings.

6.1.3 Other options

Two options, GEM [40] and MICROMEGAS [41] have recently come to our notice as possible technologies for both the preshower and veto detectors. Developments in these technologies are being closely monitored. The GEM technology is particularly attractive as the assembly process is much simpler, although the fabrication of GEM sheet requires special skill. A pad readout is a good possibility for both the options.

The main problem in these options is the possibility of fabricating unit modules large enough so that boundary effects are minimal. The present stage of developments precludes using several smaller chambers to be joined together without substantial dead spaces at the boundaries. In the preshower design one

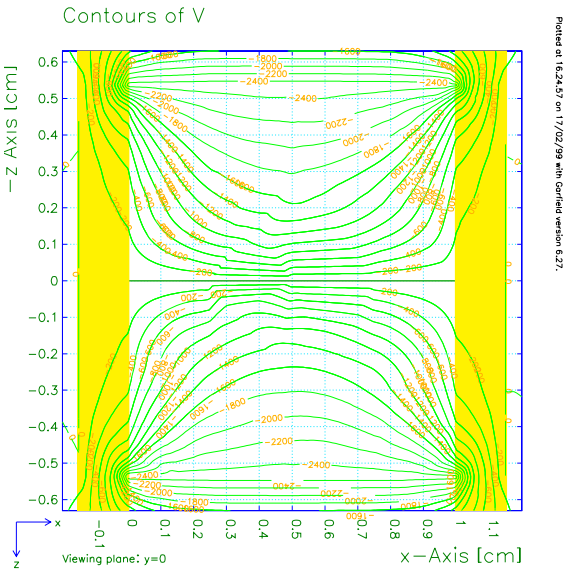

Figure 31: Equipotential lines for a hexagonal cell without guard rings.

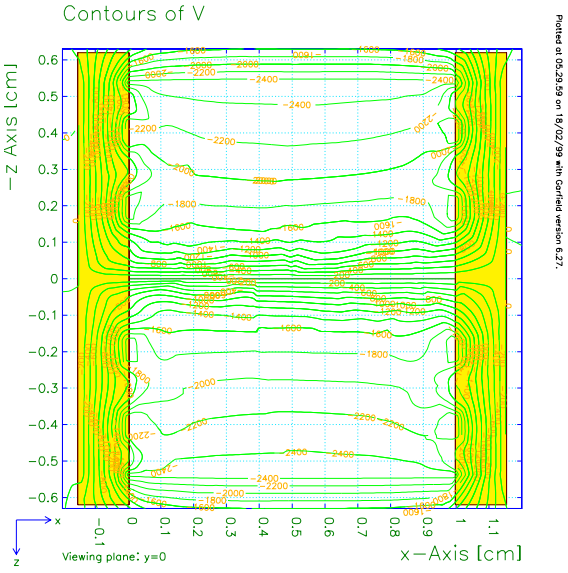

Figure 32: Equipotential lines for a hexagonal cell with guard rings.

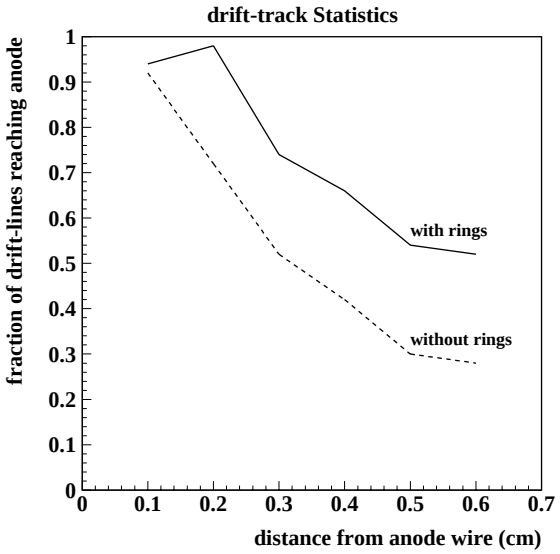

Figure 33: Fraction of electron drift lines falling on the anode wire with and without the guard rings, as indicated.

cannot use staggered layout of the modules as this introduces large volume of air trapped in between the converter and chamber planes, resulting in blow-up of photon showers. The other problem is the large gas volume, unlike the cellular chamber, and the effect of δ-rays may lead to substantial cross-talk. In addition, both the GEM and MICROMEGAS depend on expensive components, the total cost of the detector will be much higher if any of these options are used.

6.2 Detector Calibration

The calibration of the preshower PMD is performed using extensive set of test data at a number of energies using electron and pion beams. A simulation framework is developed which describes the entire set of test data as nicely as possible. A MeV-ADC calibration curve is generated from the mean positions of spectra obtained in simulation and test beams as described in detail in [6]. A comparison of test data and simulation also helps to understand features specific to the readout system and cross-talk, if any, and to parameterize the effects.

Using data from actual experiments it is possible to select MIPs with suitable algorithms and use them to study cell-to-cell gain variations. It has been found that gain variations within 10% do not affect the clustering and hadron discrimination. However for estimates of E_T^{PMD} this gain may have to be properly accounted for.

Using simulation tuned to test beam results, one can generate required thresholds needed for photon-hadron discrimination using neural network method. A robust test of the algorithm can be designed using synthetic events where photon preshower is substituted by electron test beam data and hadron signatures are also taken from test beam data. Comparison of the synthetic events with simulation for varying multiplicities will help to understand the nature of cuts to be used to obtain optimum efficiency.

6.3 Integration of the PMD in ALICE

6.3.1 Installation procedure

The installation of the detector consists of the following steps :

- fixing of I-beam support structures on the two halves of the magnet door,
- assembly of the X- and Z- movement components with hydraulic piping etc., and positioning of the detector I-beam supports,
- hanging the stainless steel support plates,
- Fixing the lead converter pieces onto the SS support plate using the prefabricated tapped holes on the backing plate.
- Positioning and fixing the special studs at appropriate locations to fix the CPV and PMD supermodules back-to-back,
- fixing the supermodules using the special bolt/nut system shown in Fig. 34. The outer threading of this bolt will be fastened to the tapped holes in the SS plate. The SMs will then be held in place with smaller (thinner) bolts inside the threaded hole.
- Fixing the preformed gas in/out SS piping on the boundary of the SS support plate. This piping is provided with a number of parallel feed points conveniently located to provide gas inlet to all supermodules in each half of the detector.

6.3.2 Cooling and ventilation

The readout electronics of the PMD will dissipate about 2 kW of heat, assuming 10 mW per channel. The average density of electronics will be approx. 10,000

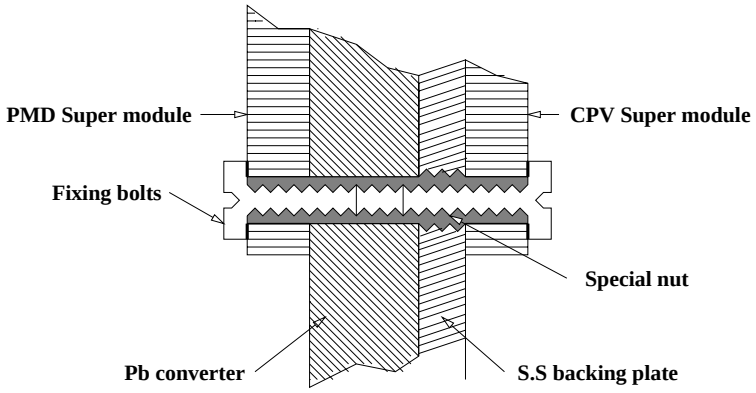

Figure 34: nut/bolt system for hanging the supermodules

channels per sq.m., although at the MCM board the chips may be closer. Forced air cooling for the front-end electronics will be required. Air vents located at the bottom of each detector plane will send forced air at requisite flow levels to remove the dissipated heat.

6.3.3 Electrical connections

Shallow plastic cable channels are provided at the boundaries of the supermodules to lay all low-voltage, high-voltage and signal cables. These are brought to the outer edge of the detector plane to be fed to the distribution boxes. The two halves of the detector have no direct linking lines between them, so that they can be moved/separated without disconnecting any of the electrical and gas lines.

6.3.4 Gas flow system

This consists of Ar – CO_2 mixing console with local/remote digital flow meters as shown in Fig. 35. The exhaust is fed through a long (20-30 meters) coiled SS capillary tube (4-5 mm dia.) avoiding silicon oil bubbles to reduce long term contamination effects. The exhaust also passes through a set of control proportional counters. Regular gain monitoring using radio-active sources warns about gas contamination, if any.

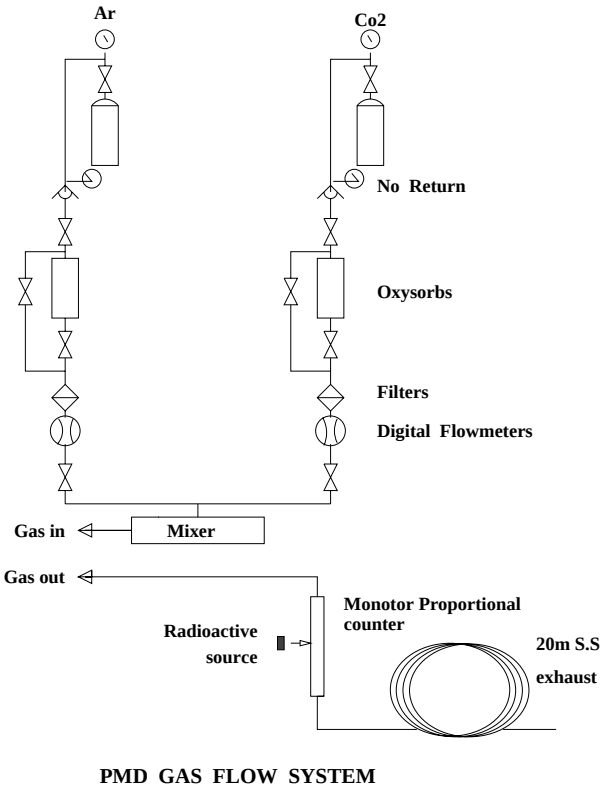

Figure 35: Gas flow system for the PMD

6.4 Access, Maintenance and Operation

The PMD integrated to the magnet door is shown in Fig. 36. Access to the magnetic cave in ALICE is provided by opening the two halves of the PMD apart by $\sim$ 2 m. This also provides access to the PMD itself for servicing.

Once the detector halves are separated, any of the detector planes are accessible by using the X-Z movements. The 1 m wide aluminium platform located near the bottom edge of the detector in the magnet hall (see Fig. 36) is designed exclusively keeping the PMD access/maintenance in mind. Small light-weight supports can be used on top of this platform to reach the upper portion of the detector, if necessary. Thus it is possible to replace defective electronics channels within a short duration of access. Access to the second plane is provided by moving the front PMD/CPV away (towards the vertex) by about 1 m.

Status of gassiplex chips, overcurrent, gas flow and contamination levels, and temperature over select places on the SMs are monitored online at regular intervals. Pedestals are measured and recorded. Test pulses are injected at regular intervals for monitoring the gain of the gassiplex and the chamber.

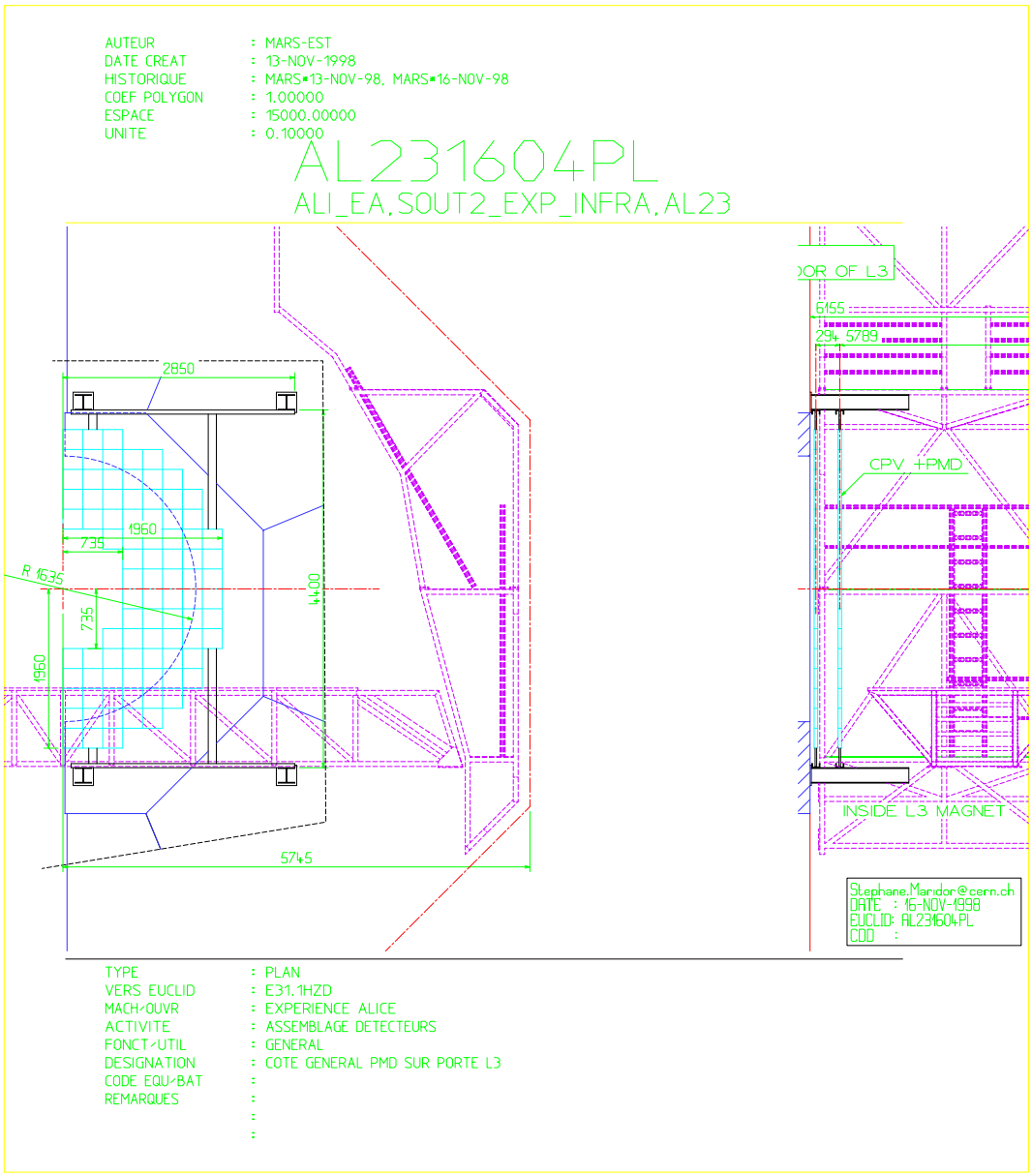

Figure 36: PMD on magnet door in ALICE.

7 Planning and Organization

7.1 Schedule

Important milestones are the following :

Completion of R&D and TDR	Dec. 1999
Pre-production prototype (unit module)	Sept. 2000
Fabrication of all UMs	Aug. 2002
Assembly of SMs	Mar. 2003
Assembly of electronics	July 2003
Transportation to CERN	Dec. 2003
Off-line tests at CERN	Mar. 2004
Installation/commissioning	May 2004

7.2 Cost Estimate

The cost of the PMD is dominated by the cost of the readout electronics. The estimates presented in Table VIII are based on the assumption of 200,000 channels of GASSIPLEX type electronics including the digitizer and the zero-suppression logic and accessories (at 3.5 CHF per channel) as quoted in [16]. The cost of the second preshower plane is not included. Additional resources will be arranged at a later stage.

TABLE VIII
Cost Estimates

Item	Cost (kCHF)
Gas counters (20 sq.m., materials/fabrication)	100
Readout Electronics	700
Converter, support structure and installation	100
TOTAL	900

7.3 Responsibilities

The responsibilities of the various groups comprising the PMD team will be the following :

VECC Calcutta : R&D, design, prototyping, fabrication of honeycomb chamber unit modules, assembly of supermodules, PCB design and fabrication, testing of the gassiplex chips, assembly of chips on MCM boards and tests, integration of the electronics with the chamber modules, transportation to CERN, development of simulation, reconstruction and analysis software.

IOP Bhubaneswar : Prototyping and fabrication of honeycomb chamber unit modules, development of simulation, reconstruction and analysis software.

PU Chandigarh : Testing of gassiplex chips, assembly of chips on MCM boards and tests, development of analysis software.

RU Jaipur : Development of simulation, reconstruction and analysis software,

JU Jammu : Testing of gassiplex chips, assembly of chips on MCM boards and tests, development of simulation, reconstruction and analysis software,

Installation and commissioning of the detector at CERN will be the joint responsibility of all the groups.

Acknowledgements

We gratefully acknowledge the help of S. Iranzo and R. Veenhof in running the maxwell and garfield simulation codes.

References

[1] ALICE Technical Proposal, CERN/LHCC 95-71, LHCC/P3, p. 117.

[2] T.K. Nayak et al., WA98 Collaboration, Quark Matter '97 proceedings, Nucl.Phys. A638 (1998) 249c.

[3] M.M. Aggarwal et al., WA93 collaboration, Phys. Lett. B403 (1997) 390.

[4] Y.P. Viyogi, ALICE Internal Note 98-52 (1998).

[5] M.M. Aggarwal et al, Nucl. Instr. Meth. A372 (1996) 143.

[6] M.M. Aggarwal et al., hep-ex/980726, Nucl. Instr. Meth. sec. A (in press).

[7] STAR Note SN-310 (1997).

[8] V. Balagura, Nucl. Instr. Meth. A368 (1995) 252.

[9] Y.P. Viyogi et al., ALICE Internal Note 95-20 (1995).

[10] S. Chattopadhyay et al., VECC/EQG/99-03, Feb. 1999, under preparation, to be submitted for ALICE Internal Note.

[11] Y. Takahashi et al., Nucl. Phys. A461 (1987) 263c.

[12] K. Rajagopal, e-print archive hep-ph/9703258.

[13] S. Chattopadhyay, Z. Ahammed and Y.P. Viyogi, Nucl. Instr. Meth. A421 (1999) 558.

[14] M.M. Aggarwal et al., VECC/EQG/99-01, Jan. 1999, submitted for ALICE Internal Note.

[15] D. Muller, Phys. Rev. C5 (1972) 2677.

[16] ALICE HMPID TDR, CERN/LHCC 98-19 (1998).

[17] R.N. Singaraju et al., VECC Internal Note VECC/EXP/98-21 (1998).

[18] M.M. Aggarwal et al, WA93 Collaboration, Phys. Rev. C58 (1998) 1146.

[19] M. Stephanov, K. Rajagopal and E. Shuryak, Phys. Rev. Lett. 81 (1998) 4816.

[20] A.A. Anselm, M.G. Ryskin, Phys. Lett. B266 (1991) 482.

[21] J. -P. Blaizot and A. Krzywcki, Phys. Rev. D46 (1992) 246.

[22] J.D. Bjorken, Int. J. Mod. Phys. A7 (1992) 4189; J.D. Bjorken, K.L. Kowalski, C.C. Taylor, "Baked Alaska", SLAC-PUB-6109, Apr., 1993.

[23] K. Rajagopal, F. Wilczek, Nucl. Phys. B399 (1993) 395.

[24] Masayuki Asakawa, Zheng Huang and Xin-Nian Wang, Phys.Rev.Lett. 74 (1995) 3126.

[25] C.M.G. Lates, Y. Fujimoto and S. Hasegawa, Phys. Rep. 65 (1980) 151.

[26] M. Ishihara, M. Maruyama and F. Takagi, Phys.Rev. C57 (1998) 1440.

[27] James Hormuzdiar and Stephen D.H. Hsu, Phys.Rev. C58 (1998) 1165.

[28] Jorgen Randrup and Robert L. Thews, Phys. Rev. D56 (1997) 4392.

[29] T.C. Brooks et al., Minimax Collab., Phys. Rev. d55 (1997) 390.

[30] M.M. Aggarwal et al., WA98 Collaboration, Phys. Lett. B420 (1998) 169.

[31] Zheng Huang, Ina Sarcevic, Robert Thews and Xin-Nian Wang, Phys. Rev. D54 (1996) 750.

[32] B.K. Nandi et al., submitted to Phys. Lett. B (1999)

[33] M.M. Aggarwal, V.S. Bhatia, A.C. Das and Y.P. Viyogi, Phys. Lett. B438 (1998) 357.

[34] A.M. Poskanzer and S.A. Voloshin, Phys. Rev. C58 (1998) 1671.

[35] J.Y. Ollitrault. Phys. Rev. D48 (1993) 1132.

[36] R. Raniwala et al., under preparation, to be submitted for ALICE Internal Note.

[37] F. Takagi, Phys. Rev. Lett. 53 (1984) 427.

[38] A.C. Das and Y.P. Viyogi, Phys. Lett. B380 (1996) 437.

[39] R. Vennhof, CERN Programme Library, entry W5050.

[40] J. Beulloch et al. Nucl. Instr. Meth. A419 (1998) 410.

[41] G. Barouch et al., Nucl. Instr. Meth. A419 (1998) 2.